STANDARD MODEL IS BEST MODEL (WORKING TITLE)

William Kennedy DiClemente

A DISSERTATION

in

Physics and Astronomy

Presented to the Faculties of The University of Pennsylvania

in Partial Fulfillment of the Requirements for the Degree of Doctor of Philosophy

2019 Last compiled: January 10, 2019

I. Joseph Kroll, Professor, Physics

Supervisor of Dissertation

Joshua Klein, Professor, Physics

Graduate Group Chairperson

Dissertation Committee

(Committee Prof. 1), Professor, Physics

(Committee Prof. 2), Associate Professor, Physics

(Committee Prof. 3), Professor, Physics

(Committee Prof. 4), Professor, Physics

I. Joseph Kroll, Professor, Physics

Standard Model is best model (working title)

Acknowledgements

I'd like to thanks the Ghosts of Penn Students Past for providing me with such an amazing thesis template.

ABSTRACT

Standard Model is best model (working title)

William Kennedy DiClemente

J. Kroll

This is the abstract text.

Contents

List of Tables

List of Figures

Preface

This is the preface. It's optional, but it's nice to give some context for the reader and stuff.

Will K. DiClemente

Philadelphia, February 2019

CHAPTER 1

Introduction

233 The Standard Model (SM)[1] has been remarkably successful...

---

[1]Here's a footnote.

Theoretical Framework

(Some example introductory text for this chapter)...

2.1 Introduction to the Standard Model

Modern particle physics is generally interpreted in terms of the Standard Model (SM). This is a quantum field theory which encapsulates our understanding of the electromagnetic, weak, and strong interactions...

2.2 Electroweak Mixing and the Higgs Field

When the theory of the electroweak interaction was first developed [4, 5], the W and Z bosons were predicted to be massless (a typical mass term in the Lagrangian would violate the SU(2) symmetry). However, these were experimentally observed to have masses...

LHC and the ATLAS Detector

3.1 The Large Hadron Collider

The Large Hadron Collider (LHC) [6] is...

3.2 The ATLAS Detector

ATLAS is a general-purpose particle detector...

3.2.1 The Inner Detector

The Inner Detector serves the primary purpose of measuring the trajectories of charged particles...

3.2.1.1 Pixel Detector

The Pixel detector consists of four cylindrical barrel layers and three disk-shaped endcap layers...

3.2.1.2 Semiconductor Tracker

The Semiconductor Tracker uses the same basic technology as the Pixels, but the fundamental unit of silicon is a larger "strip"...

3.2.1.3 Transition Radiation Tracker

The Transition Radiation Tracker is the outermost component of the ID...
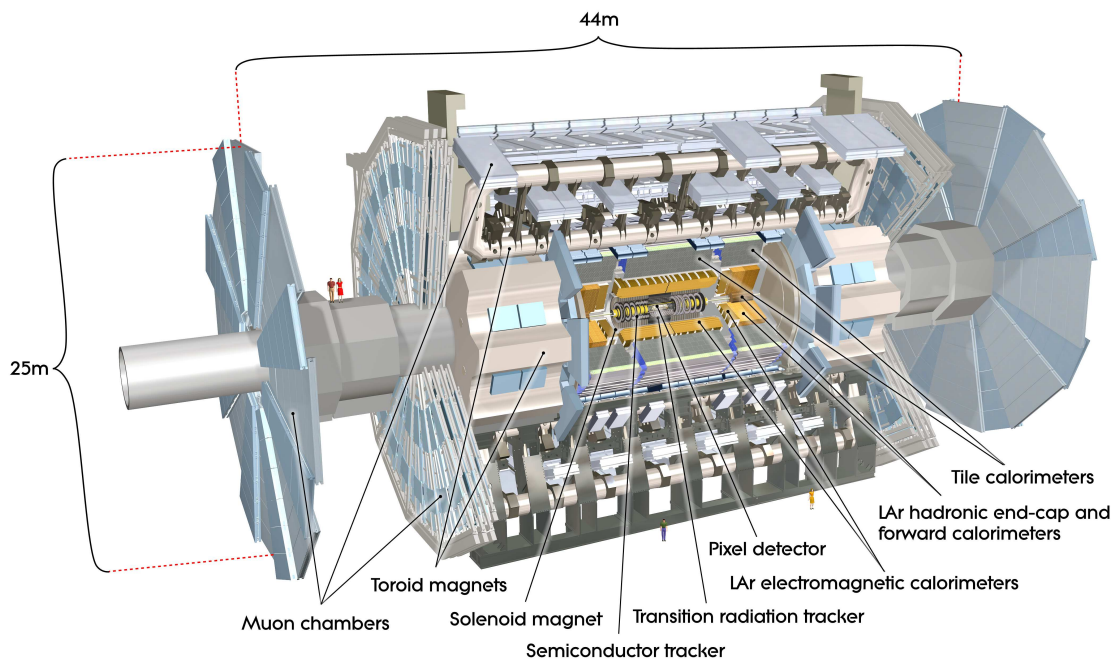
Figure 3.1: General cut-away view of the ATLAS detector [7].

3.2.2 The Calorimeters

ATLAS includes two types of calorimeter system for measuring electromagnetic and hadronic show-
ers. These are the Liquid Argon (LAr) calorimeters and the Tile calorimeters. Together, these cover
the region with $|\eta| < 4.9...$

3.2.2.1 Liquid Argon Calorimeters

The Liquid Argon system consists of...

3.2.2.2 Tile Calorimeters

The Tile calorimeter provides coverage for hadronic showers...

3.2.3 The Muon Spectrometer

Muon spectrometer stuff.

3.2.4   Particle reconstruction

Particle reconstruction algorithms

3.2.4.1   Track reconstruction

3.2.4.2   Muon reconstruction

3.2.4.3   Electron reconstruction

3.2.4.4   Jet reconstruction

Alignment of the ATLAS Inner Detector

In order for the subdetectors of the ID to operate at their designed precisions, it is essential that the locations of the sensors be known as precisely as possible. Differences between the expected and actual positions of a sensor can result in displaced particle hits and degrade track reconstruction quality. These misalignments can occur for any number of reasons, including but not limited to elemnts shifting during maintenance periods or cycles in ATLAS's magnetic field, or simply small movements during normal detector operations. Since it is not practical to physically realign hundreds of thousands of detector elements to μm precision by hand, an iterative track-based alignment algorithm is used to determine the physical positions and orientations of these elements [8]. The effects of misalignments and the steps taken to correct and monitor them are detailed in this chapter.

4.1   Effects of Misalignment

Hello world!

4.2   The Alignment Method

Hello world!

4.3   Momentum Bias Corrections

Hello world!

4.4 Alignment of the IBL

Hello world!

4.5 Alignment Monitoring

Hello world!

CHAPTER 5

Measurement of same-sign WW production at $\sqrt{s} = 13$ TeV with ATLAS

Production of same-sign W boson pairs is a particularly interesting SM process. When produced via vector boson scattering (VBS), $W^{\pm}W^{\pm}jj$ is particularly sensitive to the electroweak symmetry breaking (EWSB) mechanism as well as potential "beyond the Standard Model" (BSM) physics. $W^{\pm}W^{\pm}jj$ events can be produced via electroweak-mediated (EWK) diagrams, of which VBS is a subset, or QCD-mediated diagrams. The biggest advantage of same-sign $W^{\pm}W^{\pm}jj$ lies in its ratio of electroweak (EWK) to QCD production cross sections. Despite the opposite-sign $W^{\pm}W^{\mp}$ having a considerably larger total cross section, its EWK-mediated diagrams are considerably smaller than its QCD-mediated diagrams, while for same-sign $W^{\pm}W^{\pm}$ the ratio is approximately one to one. This makes $W^{\pm}W^{\pm}jj$ one of the best channels for studying VBS at the LHC.

The first evidence of electroweak (EWK) $W^{\pm}W^{\pm}jj$ production was seen by the ATLAS and CMS experiments at $\sqrt{s} = 8$ TeV with exesses of 3.6σ [9] and 2.0σ [10] over backgrounds, respectively. More recently, ATLAS and CMS have both observed the EWK process at $\sqrt{s} = 13$ TeV with significances of 6.9σ [11] and 5.5σ [12], respectively. The analysis presented in this chapter is based off of the ATLAS $\sqrt{s} = 13$ TeV observation and cross section measurement of EWK $W^{\pm}W^{\pm}jj$ production [11, 13].

5.0.1 Theoretical overview of vector boson scattering

VBS processes are very important to understand due to their sensitivity to the EWSB mechanism. The scattering amplitude of longitudinally polarized vector bosons grows with center-of-mass energy and ultimately violates unitarity above $\sqrt{s} = 1$ TeV in the absence of a light SM Higgs boson [14, 15].

8

319 However, once the Higgs is introduced, the divergences cancel and the cross section no longer grows

320 unbounded, as can be seen in Figure 5.1, which consists of plots from [2].
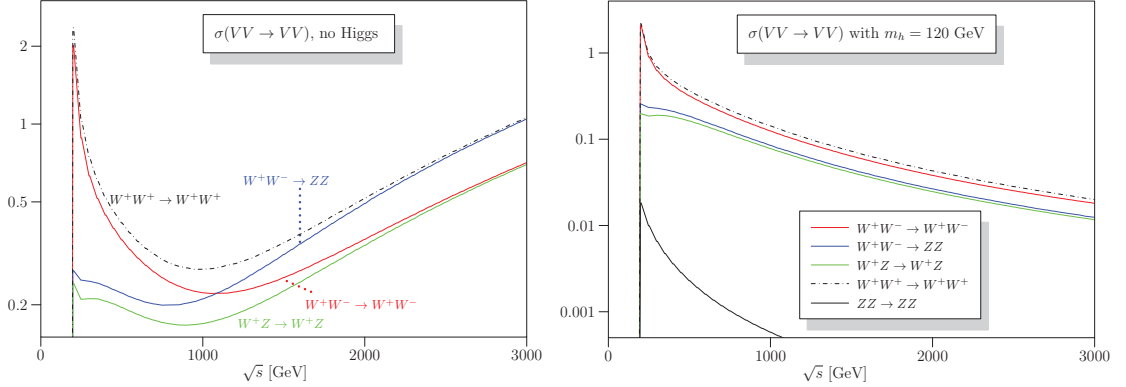
Figure 5.1: Cross sections in nb for five different scattering processes of longitudinally polarized vector bosons. Without a SM Higgs boson (left), the cross sections grow unbounded with $\sqrt{s}$; however with a 120 GeV Higgs boson (right), the cross sections no longer diverge. Plots from [2]. TODO: properly crop these plots so the rest of the pages aren't visible...

321 With the discovery of the Higgs boson in 2012 [16, 17], the EWSB mechanism can now be directly

322 studied. Due to the exchange of a Higgs in the s- and t-channel VBS diagrams ($W^{\pm}W^{\pm}jj$ specifically

323 only contains the t-channel diagram), VBS processes can directly measure properties of the Higgs.

324 For example, the high-mass tail in the VV scattering system allows an approximation of the effective

325 coupling strength of the Higgs to vector bosons that is independent of any assumptions on the Higgs

326 width [18]. Additionally, the center-of-mass energy dependence of the VV scattering can reveal

327 whether the Higgs boson unitarizes the longitudinal scattering amplitude fully or only partially [19].

328 VBS events are characterized by two quarks from the colliding protons each radiating a massive

329 vector boson which then scatter and decay in the detector. These high-momentum quarks only

330 deflect a small amount upon radiating the vector boson; as a result, they often travel very close to

331 the beam line. Ignoring the decay products of the bosons, these VBS events result in a final state

332 of two vector bosons (V) and two jets (j) at high pseudorapidities (called *forward jets*) from the

333 outgoing quarks. The shorthand $VVjj$ is used to represent this final state.

334 These $VVjj$ events can be produced via two different physical processes. The first involves

335 purely electroweak interactions in the tree-level diagrams, with $\mathcal{O}(\alpha_{\text{EWK}}) = 6$ and will be referred

336 to as *EWK production*. This can be further broken down into VBS and non-VBS production. In

337 the VBS EWK production, the scattering occurs via triple or quartic gauge couplings, as well as the

s- or t-channel exchange of a Higgs boson. The non-VBS EWK production contains the same final state of two vector bosons and two outgoing quarks, but the bosons do not scatter. Due to gauge invariance, it is not possible to separate the VBS from the non-VBS productions [20]; therefore, both are included in the signal generation and are indistinguishable from one another. The second process involves a mix of the EWK and strong interactions, of order $\mathcal{O}(\alpha_s) = 2 \otimes \mathcal{O}(\alpha_{\mathrm{EWK}}) = 4$ and will be referred to as *QCD production*. The tree-level Feynman diagrams for VBS EWK, non-VBS EWK, and QCD $VVjj$ production are found in Figures 5.2, 5.3, and 5.4, respectively.
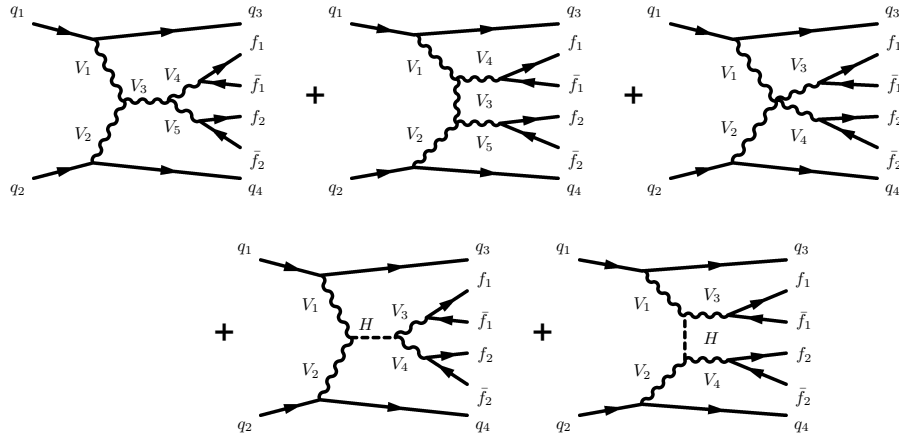
Figure 5.2: Tree-level Feynman diagrams for VBS EWK $VVjj$ production including triple gauge couplings involving W and/or Z bosons (top left and top middle), quartic gauge coupling (top right), or the exchange of a Higgs boson (s-channel bottom left and t-channel bottom right). The labels are quarks (q), fermions (f), and gauge bosons ($V = W, Z$). TODO: Crop properly
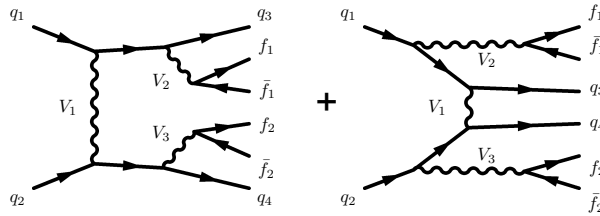
Figure 5.3: Tree-level Feynman diagrams for non-VBS EWK $VVjj$ production. The labels are quarks (q), fermions (f), and gauge bosons ($V = W, Z$). TODO: Crop properly

TODO: Continue here Using the `SHERPA` Monte Carlo (MC) generator, leading order cross sections at $\sqrt{s} = 8$ TeV are calculated for a variety of diboson processes For example, even though the total cross section of opposite-sign WW production is considerably larger than that of same-sign
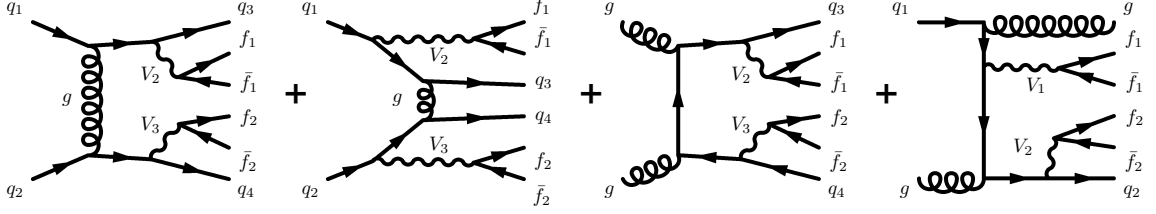
Figure 5.4: Tree-level Feynman diagrams for QCD $VVjj$ production. The labels are quarks (q), fermions (f), and gauge bosons $(V = W, Z)$. TODO: Crop properly

WW, the ratio of EWK to QCD production is approximately 3%

There are several advantages to studying the same-sign WW process specifically. The final state's net charge of ±2 helps considerably in reducing the number of background processes that can mimic the signal.

Process	σ_{EWK}	σ_{QCD}
$W^{\pm}W^{\pm} \to l^{\pm}l^{\pm}\nu\nu jj$	19.5 fb	18.8 fb
$W^{\pm}W^{\mp} \to l^{\pm}l^{\mp}\nu\nu jj$	91.3 fb	3030 fb
$W^{\pm}Z \to l^{\pm}l^{\pm}l^{\mp}\nu jj$	30.2 fb	687 fb
$ZZ \to l^{+}l^{-}\nu\nu jj$	2.4 fb	162 fb
$ZZ \to l^{+}l^{-}l^{+}l^{-}jj$	1.5 fb	106 fb

Table 5.1: Predicted cross sections for EQK and QCD production of diboson processes relevant to VBS at $\sqrt{s} = 8$ TeV. Table from [1].

5.0.2 Same-sign $W^{\pm}W^{\pm}$ scattering

The process of interest is the production of two W bosons with the same electric charge and two jets. For the purposes of this analysis, only the case where both bosons decay leptonically to electrons or muons is considered, which results in a final state with two same charge leptons, two neutrinos, and two jets.

5.1 Data and Monte Carlo samples

This analysis uses 36.1 fb^{-1} of $\sqrt{s} = 13$ TeV proton-proton collision data recorded by ATLAS during 2015 and 2016. The uncertainty in the combined integrated luminosity is 2.1%. It is derived following a methodology similar to that detailed in [21] and using the LUCID-2 detector for the baseline luminosity measurements [22] from calibration of the luminosity scale using x-y beam-separation scans.
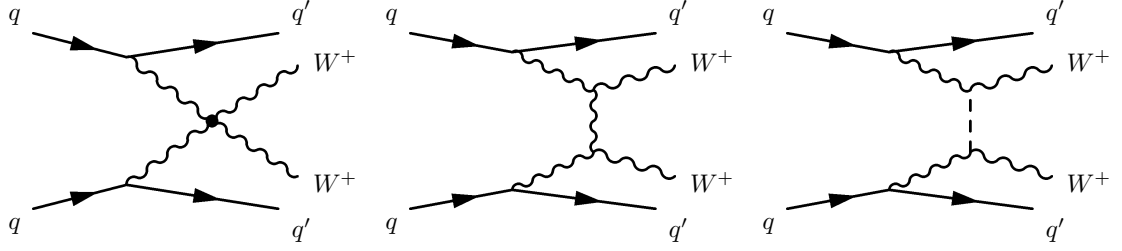
Figure 5.5: Feynman diagrams for VBS EWK production of $W^{\pm}W^{\pm}jj$ events. The leftmost diagram contains a quartic gauge coupling vertex, and the rightmost diagram contains an exchange of a Higgs boson. TODO: Make own diagrams
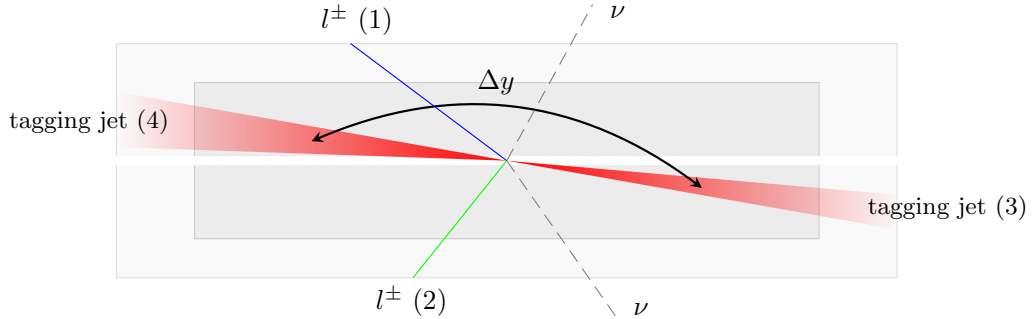
Figure 5.6: $W^{\pm}W^{\pm}jj$ VBS event topology containing two leptons (1 and 2) with the same electric charge, two neutrinos, and two forward tagging jets (3 and 4) with large rapidity separation Δy.

5.1.1   Monte Carlo samples

A number of Monte Carlo (MC) simululations are employed to model signal and background processes. In order to model the real collision data as closely as possible, each MC has been run through a full simulation of the ATLAS detector [23] in `GEANT4` [24], and events have been reconstructed using the same algorithms as the data. The simulation reproduces as closely as possible the momentum resolutions and calorimeter responses of the detector, and also includes the effects of pileup by including soft QCD interactions using `PYTHIA v8.1` [25]. The MC samples used in this analysis are detailed in this section and summarized in Table 5.2.

   The $W^{\pm}W^{\pm}jj$ samples are modeled using `SHERPA v2.2.2` [26, 27, 28] with the `NNPDF3.0` PDF set [29]. The EWK signal samples are generated by fixing the electroweak coupling constant to $\mathcal{O}(\alpha_W) = 6$, and a QCD background sample was also generated with $\mathcal{O}(\alpha_W) = 4$. `SHERPA` includes up to one parton at next-to-leading order (NLO) and up to three at leading order (LO) in the

Process	Generator	Comments
$W^{\pm}W^{\pm}jj$ (EWK)	SHERPA v2.2.2	Signal sample
$W^{\pm}W^{\pm}jj$ (EWK)	POWHEG-BOX v2	Systematics sample
$W^{\pm}W^{\pm}jj$ (QCD)	SHERPA v2.2.2	
Diboson	SHERPA v2.2.2	Both bosons decay leptonically ($llll$, $lll\nu$, $ll\nu\nu$)
	SHERPA v2.2.1	One boson decays leptonically, the other hadronically
Triboson	SHERPA v2.1.1	
W+jets	SHERPA v2.2.1	
Z+jets	Madgraph5_aMC@NLO	
$V\gamma$	SHERPA v2.1.1	
$V\gamma jj$ (EWK)	SHERPA v2.2.4	
$t\bar{t}V$	Madgraph5_aMC@NLO	
$t\bar{t}$	POWHEG-BOX v2	
Single top	POWHEG-BOX v1	EWK t-, s-, & Wt-channels

Table 5.2: Summary of MC samples used in the analysis.

strong coupling constant α_s. A second $W^{\pm}W^{\pm}jj$ EWK sample is generated using POWHEG-BOX v2 [30] with the NNPDF3.0 PDF set and at NLO accuracy. This sample is only used for systematic studies, as POWHEG-BOX does not include resonant triboson contributions in its matrix element, which are non-negligible at NLO [31].

Diboson processes (VV where $V = W, Z$) are simulated with SHERPA v2.2.2 for mixed hadronic and leptonic decays and SHERPA v2.2.1 for fully leptonic decays of the bosons. Similarly, triboson (VVV) and $V\gamma$ processes are simulated using SHERPA v2.1.1 with up to one parton at NLO and up to three at LO. W+jets processes are simulated with SHERPA2.2.1 with up to two partons at NLO and four at LO. All the above SHERPA samples use the NNPDF3.0 PDF set and SHERPA's own parton showering. The Z+jets events are generated with Madgraph5_aMC@NLO [32] at LO and interfaced with PYTHIA v8.1 for parton showering.

$t\bar{t}$ events are generated using POWHEG-BOX v2 with the CT10 PDF set [33]. $t\bar{t}V$ samples are generated at NLO with Madgraph5_aMC@NLO and the NNPDF3.0 PDF set interfaced with PYTHIA v8 for parton showering. Finally, single top events are generated with POWHEG-BOX v1 and the CT10f4 PDF set interfaced with PYTHIA6 [34] for parton showering.

5.2   Object and event selection

This section details the selection criteria for objects used in the analysis as well as the selection for signal events.

5.2.1   Object selection

Muons, electrons, and jets all must pass strict selection requirements to ensure that only high quality, well measured objects are used. For leptons, a baseline selection is defined (called the *preselection*), which all leptons must pass in order to be considered for the analysis. This preselection is an intentionally loose set of criteria in order to have high acceptance for rejecting backgrounds with additional leptons (i.e. $WZ \rightarrow 3l\nu jj$). Signal leptons are then required to satisfy a much tighter *signal selection* aimed at suppressing backgrounds from non-prompt or fake leptons. A third set of lepton selection criteria, the *loose selection*, defines a sample enriched in non-prompt leptons, and it is used in the fake factor method for estimating the non-prompt background, discussed in detail in Section 5.3.2. Jets are only required to pass one set of selection criteria. These selections are detailed in the following sections and summarized in Table 5.3 for muons, Table 5.4 for electrons, and Table 5.5 for jets.

5.2.1.1   Muon candidate selection

Cuts on muon p_T serve to reject low momentum leptons from background processes and additional collisions from pileup events. Preselected muons must have $p_T > 6$ GeV and signal muons $p_T > 27$ GeV. The p_T requirement for loose muons is lower than for signal muons, $p_T > 15$ GeV, for reasons that are discussed in Section 5.3.2. TODO: reference proper subsection when it's done Muons are required to fall within the detector's η acceptance: $|\eta| < 2.7$ for preselected muons, which is tightened to $|\eta| < 2.5$ for the signal muons.

Cuts on the transverse and longitudinal impact parameters are applied to ensure that the candidate muon originated from the primary particle interaction and not some other source, such as a heavy flavor decay. The preselection and the loose selection both have looser requirements on the transverse impact parameter significance (d_0/σ_{d_0}) than the signal selection; all three have the same requirement on the transverse impact paramter ($|z_0 \times \sin\theta|$).

Finally, the muon candidates are required to pass a particle identification and an isolation criteria as defined in [35]. The methods used in constructing the identification and isolation workingpoints are described in more detail in Section 3.2.4.2. The muon identification serves to select prompt muons with high efficiency and well measured momenta.This analysis uses two different workingpoints, `Loose` for preselected muons and `Medium` for loose and signal muons, where `Medium` muons are a tighter subset of those that pass the `Loose` requirement. Muon isolation is a measurement of detector activity around the muon candidate, and it is measured with both track-based and calorimeter-

based variables. The isolation workingpoint used for the signal muons, `Gradient`, is defined such that there is 90% or better background rejection efficiency for 25 GeV muons, and 99% efficiency at 60 GeV. There is no minimum isolation requirement for preselected or loose muons. Loose muons are additionally required to fail one or both of the signal transverse impact parameter cut and signal isolation requirement.

<div align="center">

Muon preselection

Momentum cut	$p_{\mathrm{T}} > 6$ GeV
Angular acceptance	$|\eta| < 2.7$
Longitudinal impact parameter	$|z_0 \times \sin\theta| < 0.5$ mm
Transverse impact parameter	$d_0/\sigma_{d_0} < 10$
Particle identification	`Loose`

Muon signal selection

Momentum cut	$p_{\mathrm{T}} > 27$ GeV
Angular acceptance	$|\eta| < 2.5$
Longitudinal impact parameter	$|z_0 \times \sin\theta| < 0.5$ mm
Transverse impact parameter	$d_0/\sigma_{d_0} < 3$
Particle identification	`Medium`
Particle isolation	`Gradient`

Muon loose selection

Momentum cut	$p_{\mathrm{T}} > 15$ GeV
Angular acceptance	$|\eta| < 2.5$
Longitudinal impact parameter	$|z_0 \times \sin\theta| < 0.5$ mm
Transverse impact parameter	$d_0/\sigma_{d_0} < 10$
Particle identification	`Medium`
Fail signal transverse impact parameter and/or isolation cuts	

</div>

Table 5.3: Muon selection criteria. All muons are required to pass the preselection (top), and then either the signal (middle) or loose (bottom) criteria is applied to the preselected electrons.

5.2.1.2   Electron candidate selection

The electron candidate selections are very similar to those for muons. The p_{T} cut starts at $p_{\mathrm{T}} > 6$ GeV for the preselection, increases to $p_{\mathrm{T}} > 15$ GeV for loose electrons, and finally to $p_{\mathrm{T}} > 27$ GeV for signal electrons. The $|\eta|$ cut for electrons requires $|\eta| < 2.47$ for all electrons, with the region $1.37 \leq |\eta| \leq 1.52$ removed from loose and signal electrons. This region is where the electromagnetic calorimeter transitions from the barrel to the endcaps and is not fully instrumented. Both the transverse and longitudinal impact parameter cuts are the same for all electron selections.

The electron particle identification uses a multivariate likelihood technique (LH) [36] detailed in Section 3.2.4.3. Preselected electrons must pass the loosest LH workingpoint `LooseLH` with an additional requirement that there be a reconstructed track hit in the first layer of the pixel detector (a so-called B-layer hit). The LH requirement for the loose and signal electrons the tighness of the identification using `MediumLH` and `TightLH`, respectively. As for isolation, the `Gradient` workingpoint is required for signal electrons only. The loose electrons must fail one or both of the signal identification and isolation requirements.

Electron preselection	
Momentum cut	$p_{\mathrm{T}} > 6$ GeV
Angular acceptance	$|\eta| < 2.47$
Longitudinal impact parameter	$|z_0 \times \sin\theta| < 0.5$ mm
Transverse impact parameter	$d_0/\sigma_{d_0} < 5$
Particle identification	`LooseLH` $+$ B-layer hit

Electron signal selection	
Momentum cut	$p_{\mathrm{T}} > 27$ GeV
Angular acceptance	$|\eta| < 2.47$, excluding $1.37 \leq |\eta| \leq 1.52$
Longitudinal impact parameter	$|z_0 \times \sin\theta| < 0.5$ mm
Transverse impact parameter	$d_0/\sigma_{d_0} < 5$
Particle identification	`TightLH`
Particle isolation	`Gradient`

Electron loose selection	
Momentum cut	$p_{\mathrm{T}} > 15$ GeV
Angular acceptance	$|\eta| < 2.47$, excluding $1.37 \leq |\eta| \leq 1.52$
Longitudinal impact parameter	$|z_0 \times \sin\theta| < 0.5$ mm
Transverse impact parameter	$d_0/\sigma_{d_0} < 5$
Particle identification	`MediumLH`
Fail signal identification and/or isolation cuts	

Table 5.4: Electron selection criteria. All electrons are required to pass the preselection (top), and then either the signal (middle) or loose (bottom) criteria is applied to the preselected electrons.

5.2.1.3   Jet candidate selection

The final objects that need to pass selection are jets. Jets are clustered using the anti-k_t algorithm [37] within a radius of $\Delta R = 0.4$. The jets are then calibrated using E_{T}- and η-dependent correction factors that are trained using MC simulations [38]. These calibrated jets are then re-

447 quired to have $p_\mathrm{T} > 30$ GeV if they lie in the forward regions of the detector $(2.4 < |\eta| < 4.5)$ and
448 $p_\mathrm{T} > 25$ GeV in the central region $(|\eta| \leq 2.4)$. In order to suppress pileup jets, the so-called jet-
449 vertex-tagger (JVT) discriminant associates a jet with the primary interaction vertex [39]; central
450 jets with $p_\mathrm{T} > 60$ GeV are required to pass the `Medium` JVT workingpoint, which corresponds to
451 an average efficiency of over 92%. Finally, the jets are required to be separated by selected prompt
452 leptons by at least $\Delta R(j, l) > 0.3$.

Jet selection	
Momentum cut	$p_\mathrm{T} > 30$ GeV for $2.4 < |\eta| < 4.5$
	$p_\mathrm{T} > 60$ GeV for $|\eta| < 2.4$
JVT cut	`Medium`
Jet-lepton separation	$\Delta R(j, l) > 0.3$

Table 5.5:

5.2.1.4   Treatment of overlapping objects

454 In the event that one or more objects are reconstructed very close to each other, there is the
455 possiblity for double-counting if both originated from the same object. The procedure by which
456 this ambiguity is resolved is called *overlap removal* (OR). The standard ATLAS recommendation
457 for OR is implemented in this analysis [40, 41] and is summarized in Table 5.6.

458   Since electrons leave a shower in the EM calorimeter, every electron has a jet associated with
459 it. Therefore, any jets close to an electron (within $\Delta R(e, j) < 0.2$) are rejected due to the high
460 probability that they are the same object. On the other hand, when jets and electrons overlap
461 within a large radius of $0.2 < \Delta R(e, j) < 0.4$, it is likely that the electron and jet both are part of
462 a heavy-flavor decay, and the electron is rejected.

463   High energy muons can produce photons via bremsstrahlung radiation or collinear final state
464 radiation which results in a nearby energy deposit in the calorimeters. Non-prompt muons from
465 hadronic decays produce a similar signature; however, in this case the jet has a higher track multiplic-
466 ity in the ID. It is possible to address both cases by rejecting the jet when the ID track multiplicity
467 is less than three and otherwise rejecting the muon for jets and muons within $\Delta R(\mu, j) < 0.4$.

468   In addition to the case above where muon bremsstrahlung results in a nearby reconstructed jet,
469 the ID track from the muon and the calorimeter energy deposit can lead to it bein reconstructed
470 as an electron. In this case, if both a muon and an electron share a track in the ID, the muon is
471 kept and the electron is rejected, unless the muon is calorimeter-tagged[2], in which case the muon is

---

[2]A calorimeter-tagged (CT) muon is a muon that is identified by matching an ID track to a calorimeter energy

removed in favor of the electron.

Overlap	Check	Result (remove $\rightarrow$ keep)
Electron & Jet	$\Delta R(e, j) < 0.2$	Jet $\rightarrow$ electron
	$0.2 < \Delta R(e, j) < 0.4$	Electron $\rightarrow$ jet
Muon & Jet	$\Delta R(\mu, j) < 0.4$ and Jet $N_{\text{ID tracks}} < 3$	Jet $\rightarrow$ muon
	$\Delta R(\mu, j) < 0.4$ and Jet $N_{\text{ID tracks}} \geq 3$	Muon $\rightarrow$ jet
Electron & Muon	Shared ID track	Electron $\rightarrow$ muon
	Shared ID track & muon is calo-tagged	Muon $\rightarrow$ electron

Table 5.6: Summary of the overlap removal procedure used in the analysis. If the criteria in the "check" column is met, in the "result" column, the object on the left of the arrow is removed in favor of the object on the right.

5.2.2 Signal event selection

After the objects have been selected, cuts are applied on a per-event level to select $W^{\pm}W^{\pm}jj$ signal events. The event selection is summarized in Table 5.8 and is detailed in this section. It includes the results of an optimization performed using a multidimensional grid scan.

The initial event selection begins by choosing events that pass one or more of the trigger requirements listed in Table 5.7. At least one signal lepton is "matched" to a passed trigger in order to ensure that it was indeed a signal lepton that fired the trigger. A collection of *event cleaning* cuts must also be passed in order to remove events collected during periods in which one or more components of the detector was not operating optimally. Finally, the events are required to contain at least one interaction vertex. An event can have multiple reconstructed vertices from additional proton-proton collisions that occurred in the same bunch crossing. In this case, the *primary vertex* is determined by choosing the vertex with the largest sum of the p_{T}^2 of its associated tracks.

	2015 data	2016 data
Electrons	$p_{\text{T}} > 24$ GeV and `Medium` ID	$p_{\text{T}} > 26$ GeV and `Tight` ID and `Loose` isolation
	$p_{\text{T}} > 60$ GeV and `Medium` ID	$p_{\text{T}} > 60$ GeV and `Medium` ID
	$p_{\text{T}} > 120$ GeV and `Loose` ID	$p_{\text{T}} > 140$ GeV and `Loose` ID
Muons	$p_{\text{T}} > 20$ GeV and `Loose` isolation	$p_{\text{T}} > 26$ GeV and `Medium` isolation
	$p_{\text{T}} > 50$ GeV	$p_{\text{T}} > 50$ GeV

Table 5.7: Summary of trigger requirements for electrons and muons for $\sqrt{s} = 13$ TeV data collected in 2015 and 2016. At least one of the triggers must be satisfied.

---

deposit. CT muons have relatively low reconstruction efficiency compared to those measured by the MS, but can be used to recover acceptance in regions of the detector where the MS does not have full coverage [35].

Events are then required to contain exactly two signal leptons with the same electric charge. The dilepton pair must have a combined invariant mass of $m_{ll} \geq 20$ GeV in order to suppress low mass Drell-Yan backgrounds. Two additional selections are applied to events in the ee-channel: both electrons are required to have $|\eta| < 1.37$ with an invariant mass at least 15 GeV away from the Z-boson mass to reduce events where one electron is reconstructed with the wrong charge (this background will be discussed in more detail in Section 5.3 TODO: Replace with proper subsection once it's written). To suppress backgrounds from events with more than two leptons, events with more than two leptons passing the preselection are vetoed.

Missing transverse energy ($E_{\mathrm{T}}^{\mathrm{miss}}$) represents any particles that escape the detector without being measured, such as neutrinos, and is defined as the magnitude of the vector sum of transverse momenta of all reconstructed objects. It can be difficult to calculate accurately, as it involves measurements from all subsystems within the detector, and it is sensitive to any corrections that may be applied to the reconstructed physics objects [42]. These corrections, including the momentum smearing for muons, energy scale and smearing for electrons, and jet calibrations, are propagated to the $E_{\mathrm{T}}^{\mathrm{miss}}$ calculation. Events are required to contain $E_{\mathrm{T}}^{\mathrm{miss}} > 30$ GeV in order to account for the two neutrinos from the W boson decays.

At least two jets are required. The leading and subleading jets must have $p_{\mathrm{T}} > 65$ GeV and $p_{\mathrm{T}} > 35$ GeV, respectively, and are referred to as the *tagging jets*. Events are vetoed if they contain one or more jets that have been tagged as a b-jet to suppress backgrounds from heavy flavor decays (especially top quark events). The b-tagging algorithm used by ATLAS is a boosted decision tree (BDT) called MV2c10, and this analysis uses a workingpoint with 85% efficiency [43].

Finally, cuts are applied on the VBS signature outlined in Section 5.0.2. The tagging jets are required to have a dijet invariant mass $m_{jj} > 200$ GeV and be separated in rapidity by $|\Delta y_{jj}| > 2.0$. This preferentially selects the VBS EWK events over the QCD-produced $W^{\pm}W^{\pm}jj$ events.

5.3 Background estimations

Hello world!

5.3.1 Reduction of WZ background using custom overlap removal

The dominant source of prompt background in this analysis comes from WZ events where both bosons decay leptonically. Traditionally, the background is dealt with by imposing a veto on any event with a third lepton passing some loose identification criteria (the so-called *trilepton veto*). In

Event selection

Event preselection	Pass at least one trigger with a matched lepton
	Pass event cleaning
	At least one reconstructed vertex
Lepton selection	Exactly two leptons passing signal selection
	Both signal leptons with the same electric charge
	$|\eta| < 1.37$ and $|M_{ee} - M_Z| > 15$ GeV (ee-channel only)
	Veto events with more than two preselected leptons
Missing transverse energy	$E_{\mathrm{T}}^{\mathrm{miss}} \geq 30$ GeV
Jet selection	At least two jets
	Leading jet $p_{\mathrm{T}} > 65$ GeV
	Subleading jet $p_{\mathrm{T}} > 35$ GeV
	$m_{jj} > 200$ GeV
	b-jet veto
	$|\Delta y_{jj}| > 2.0$

Table 5.8: The signal event selection

the case of this analysis, if one or more leptons (in addition to the two signal leptons) passed the preselection criteria, the event would be rejected. However, WZ events can still enter the signal region if one of the leptons fails the veto selection or falls outside of the detector's acceptance.

In order to understand the sources of WZ events that are not removed by the trilepton veto, a study was performed on truth-level leptons[3] on $W^{\pm}W^{\pm}jj$ and WZ MC samples. Events with three truth leptons were selected, and each was matched to its reconstruction-level partner by finding the closest $\Delta R(\mathrm{truth, reco})$ and $\Delta p_{\mathrm{T,truth,reco}}$ match. For events surviving the trilepton veto, the two signal leptons were removed, and the remaining leptons represent real leptons that failed to be selected for the veto. Between 40-50% of these leptons fell outside of the eta acceptance of the analysis (see Figure 5.7) and were unrecoverable. The second largest source of leptons failing the preselection was the OR, defined in Section 5.2.1.4. The standard OF procedure appeared to be too aggressive in removing leptons in favor of jets, causing many three lepton events to "lose" their third lepton and pass the trilepton veto. Therefore a *Custom OR* was investigated which would replace the standard OR in the preselection and allow for better WZ rejection by removing fewer third leptons.

TODO: Mention how the extra leptons in the $W^{\pm}W^{\pm}jj$ are background leptons since there are only 2 from the main decay

In order to construct a "custom" OR, a new quantity is defined between a lepton (l) and a nearby

---

[3]Truth particles are the particles produced directly by the MC generator before being passed through the full detector simulation, at which point they are considered *reconstruction-level* (or *reco-level*) particles.
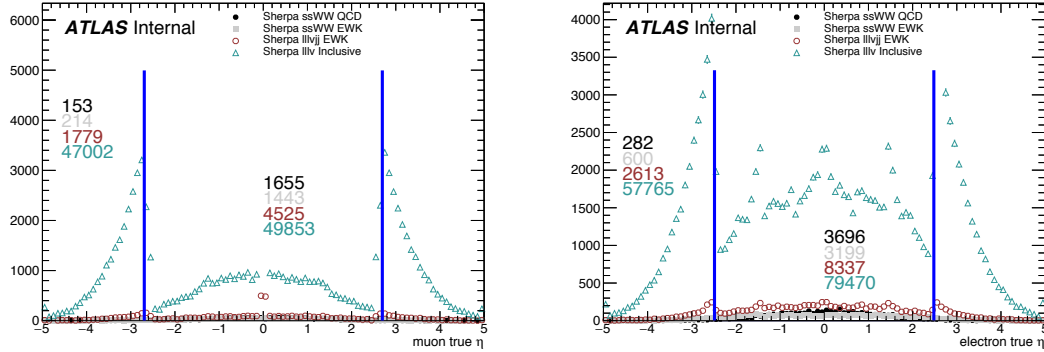
Figure 5.7: Pseudorapidity (η) distributions of truth muons (top) and electrons (bottom) for Sherpa $W^{\pm}W^{\pm}jj$ and WZ MC samples. The blue vertical lines represent the allowed η range for each lepton flavor. The numbers correspond to the number of raw MC events that fall within and outside of the allowed η range for each MC sample.

533   jet (j)

$$p_{\mathrm{T,ratio}}(l, j) = \frac{p_{\mathrm{T}l}}{p_{\mathrm{T}j}} \tag{5.1}$$

534   which, along with $\Delta R(l, j)$, will allow for more third leptons to pass the preselection. The idea

535   behind including $p_{\mathrm{T,ratio}}$ is to be able to preferentially remove background leptons originating from

536   jets (i.e. those that carry a low percentage of the total jet momentum) instead of removing *any*

537   lepton near to jet. The distributions of $p_{\mathrm{T,ratio}}$ and the associated efficiency curves for muons and

538   electrons can be found in Figures 5.8 and 5.10, respectively, and the distributions for $\Delta R(\mu, j)$ for

539   muons can be found in Figure 5.9. Since all electrons have an associated jet in the calorimeters, the

540   $\Delta R(e, j)$ variable is not a good quantity to use for this custom OR.

541   A workingpoint for the Custom OR was chosen by requiring 90% signal retention for muons

542   and 90% background rejection for electrons. The cut on electrons was allowed to be much tighter

543   because the number of signal events with a third electron is considerably smaller than for muons.

544   It should be re-emphasized the signal events that are present in Figures 5.8-5.10 do not represent

545   the full set of signal events, but only those with a real third lepton (which must come from some

546   source other than the signal $W^{\pm}W^{\pm}jj$ process). For muons, an or of $p_{\mathrm{T,ratio}}(\mu, j)$ and $\Delta R(\mu, j)$ is

547   used to maximize the third lepton acceptance due to correlations between the quantities, as shown

548   in Figure 5.11; for electrons, only a cut on $p_{\mathrm{T,ratio}}(e, j)$ is used. The Custom OR workingpoint is

549   outlined in Table 5.9.

550   Tests of the performance of the Custom OR looked promising, with approximately 20% reduction
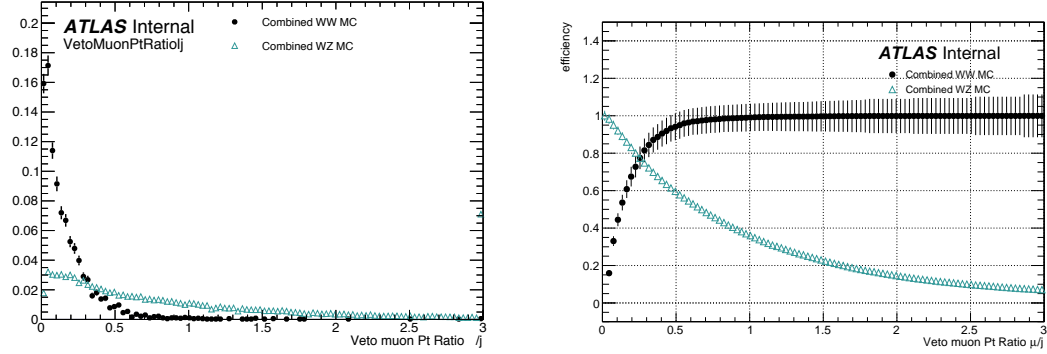
Figure 5.8: Distributions of $p_{T,\text{ratio}}(\mu, j)$ for EWK and QCD $W^{\pm}W^{\pm}jj$ signal (black) and WZ background (teal) for truth-matched third muons in events that pass the trilepton veto. Both distributions are normalized to unit area. The associated efficiency curves are on the right where efficiency is defined as the percentage of total events that would pass a cut on $p_{T,\text{ratio}}(\mu, j)$ at a given value on the x-axis.
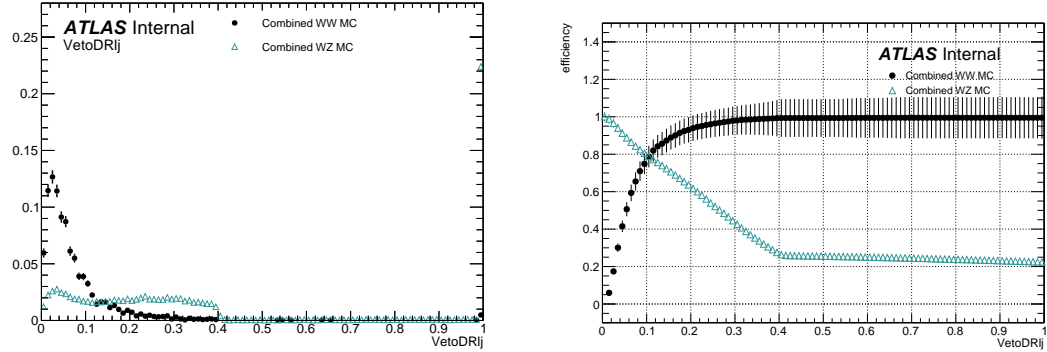
Figure 5.9: Distributions of $\Delta R(\mu, j)$ for EWK and QCD $W^{\pm}W^{\pm}jj$ signal (black) and WZ background (teal) for truth-matched third muons in events that pass the trilepton veto. Both distributions are normalized to unit area. The associated efficiency curves are on the right where efficiency is defined as the percentage of total events that would pass a cut on $\Delta R(\mu, j)$ at a given value on the x-axis.

Custom OR Definition	
Muons	$p_{T,\text{ratio}}(\mu, j) > 0.40$ or $\Delta R(\mu, j) > 0.15$
Electrons	$p_{T,\text{ratio}}(e, j) > 0.18$

Table 5.9: Custom OR definition. Leptons must pass this selection in order to be counted for the trilepton veto.
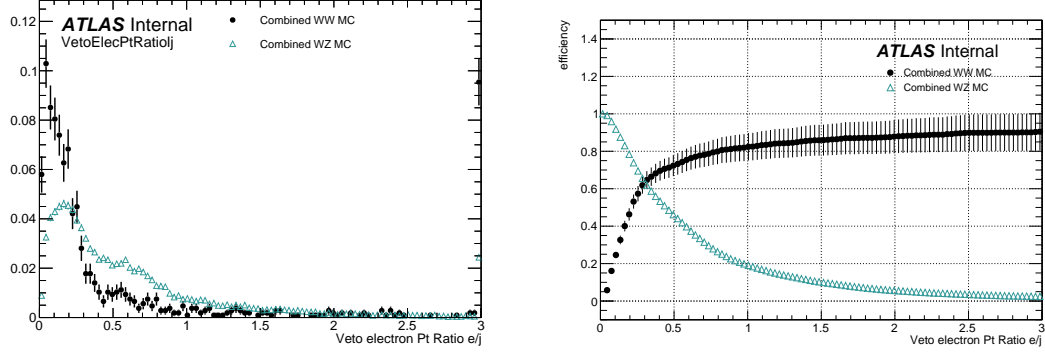
Figure 5.10: Distributions of $p_{\text{T,ratio}}(e, j)$ for EWK and QCD $W^\pm W^\pm jj$ signal (black) and WZ background (teal) for truth-matched third electrons in events that pass the trilepton veto. Both distributions are normalized to unit area. The associated efficiency curves are on the right where efficiency is defined as the percentage of total events that would pass a cut on $p_{\text{T,ratio}}(e, j)$ at a given value on the x-axis.
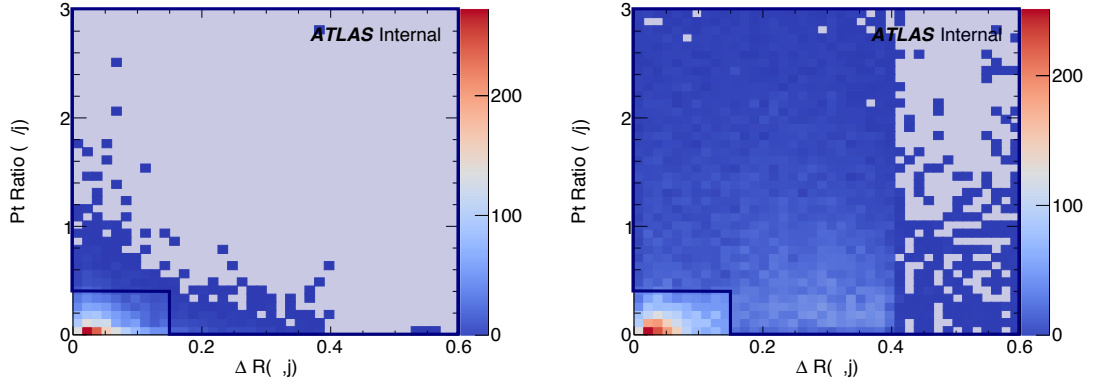
Figure 5.11: Two-dimensional plots of $p_{\text{T,ratio}}(\mu, j)$ vs $\Delta R(\mu, j)$ for truth-matched third muons in events that pass the trilepton veto for EWK and QCD $W^\pm W^\pm jj$ signal (left) and WZ background (right). The blue overlay indicates the area in which the third leptons will pass the custom OR and result in the event failing the trilepton veto.

in WZ background compared to less than 2% signal loss in the signal region. Unfortunately, due to differences between the primary analysis framework and the one used for testing, in practice the gains in WZ rejection were not nearly as substantial, and ultimately the Custom OR was dropped from the final analysis. However, it is still a potentially useful tool for improving background rejection via lepton number vetoes in analyses with overly aggressive OR procedures.

5.3.2   Fake factor method

fake factor method

5.4   Cross section measurement

Hello world!

5.5   Results

Results

CHAPTER 6

Prospects for same-sign WW at the High Luminosity LHC

On December 3, 2018, Run 2 of the LHC officialy ended, and the collider was shut down to begin the first of two scheduled extended maintenance periods [44]. During these two long shutdowns, the Phase-I and Phase-II upgrades of the LHC and ATLAS will occur in order to prepare for the High-Luminosity LHC (HL-LHC) which is scheduled to begin operation in 2026 [45].

The HL-LHC is planned to run at a center-of-mass energy of $\sqrt{s} = 14$ TeV with an instantaneous luminosity of $\mathcal{L} = 5 \times 10^{34}$ cm^{-2}s^{-1} with up to 200 collisions per beam-crossing. Over the course of operation, the HL-LHC is expected to collect a total integrated luminosity of $\mathcal{L} = 3000$ fb^{-1} by 2035 [46].

These run conditions are much harsher than what ATLAS has experienced so far, and as a result there are several planned upgrades to the detector. Most notably, the entire ID will be replaced with an all-silicon tracker which will extend the coverage from $|\eta| \leq 2.7$ up to $|\eta| \leq 4.0$. This will allow for reconstruction of charged particle tracks which can in turn be matched to clusters in the calorimeters for electron identification or forward jet tagging [47].

The upgraded detector combined with the higher beam energy and the considerable increase in integrated luminosity means that many analyses with low signal statistics in Run 2 have the potential to be greatly improved with the HL-LHC. While the ATLAS 13 TeV $W^{\pm}W^{\pm}jj$ cross section measurement certainly did not suffer greatly from low statistics TODO: –reword–, the accuracy of the measurement can still be improved at the HL-LHC. Of particular interest is the longitudinal polarization of the W bosons due to its sensitivity to electroweak symmetry breaking [48].

The analysis detailed in this chapter is based off of the 2018 public ATLAS $W^{\pm}W^{\pm}jj$ prospects

study [49] which is itself an extension of the 2017 ATLAS study [50]. TODO: mention CMS's study + yellow report?

6.0.1   Analysis Overview

The experimental signature of interest here is identical to the 13 TeV analysis detailed in Chapter 5: two prompt leptons (electrons or muons) with the same charge, missing transverse energy, and two jets. Once again the two leading jets are required to have a large angular separation and a high combined invariant mass to preferentially select EWK VBS production over QCD $W^\pm W^\pm jj$ events.

Background processes that can mimic the signal are again similar to the 13 TeV analysis. The dominant source of prompt background from WZ+jets events where both bosons decay leptonically. If the lepton from the Z-decay with opposite charge from the W falls outside of the detector acceptance or is not identified, the remainder could appear to be a $W^\pm W^\pm jj$ signal event. To a lesser extent, ZZ+jets events can enter the signal region in much the same way provided two leptons are "lost". Other prompt sources include $t\bar{t} + V$ and and multiple parton interactions, however these processes do not contribute much. The upgrades to the ATLAS detector are expected to reduce the size of these prompt contributions due in large part to the increased detector acceptance from the forward tracking. Jets mis-reconstructed as leptons or leptons from hacronic decays (such as $t\bar{t}$ and W+jets production) comprise the non-prompt lepton background. Lastly, events with two prompt, opposite-charge electrons can contribute provided one of the electrons is mis-reconstructed as the wrong charge.

In this analysis, the EWK production of $W^\pm W^\pm jj$ is studied in the context of the planned HL-LHC run conditions and upgraded ATLAS detector. An optimized event selection (referred to as the *optimized selection*) is also explored in an effort to gain increased signal significance over the *default selection*. The cross section of the inclusive EWK production is measured for both the default and optimized selections, and the extraction of the longitudinal scattering significance is measured with the optimized selection.

6.1   Theoretical motivation

The theoretical motivation for studying the ssWW process is detailed in Section 5.0.1. TODO: Rewrite this section referencing the main description in the 13tev section. Maybe just turn this into a 1 or 2 sentence refresher The particular interest in polarization is the potential for the scattering amplitude of longitudinally polarized weak bosons to diverge linearly as the center of mass energy

increases, ultimately violating unitarity around 1 TeV [14]. In the Standard Model, the Higgs boson cancels these divergences. However, as the Higgs is recently discovered it is still extremely to study the mechanism of electroweak symmetry breaking (EWSB), and the longitudinal scattering of W bosons is expected to be one of the most sensitive tests of EWSB [48].

6.1.1 Experimental sensitivity to longitudinal polarization

TODO: mention that since there are so many polarization possibilities, a large integrated luminosity is needed to measure just one of them individually There are three possible polarization states for a massive vector boson: two transverse (+ or −) and one longitudinal (0). Therefore, in a system with two W bosons, the overall polarization can be purely longitudinal (00), purely transverse (++, −−, and +−), or mixed (+0 and −0). The three combinations will be referred to as LL, TT, and LT respectively.

In order extract the longitudinal scattering component, it is necessary to find variables that distinguish the LL from the TT and LT. Several variables were studied, and those with the best discriminating power between the polarizations were the leading and subleading lepton p_T as well as the azimuthal separation ($|\Delta\phi_{jj}|$) of the two VBS jets. The LL events preferred lower p_T for both signal leptons (see Figure 6.1), which motivates keeping these two cuts as low as possible in the event selection in order to preserve as much longitudinal polarization as possible. In the case of $|\Delta\phi_{jj}|$, the LL events generally had a larger dijet separation (see Figure 6.2), and this variable is used in a binned likelihood fit to extract the longitudinal scattering significance.

6.2 Monte Carlo samples

As no real HL-LHC data will be available for many years, all processes in this prospects study must be simulated using Monte Carlo (MC) generators. Signal and background processes were generated at $\sqrt{s} = 14$ TeV, and the event yields scaled to the anticipated HL-LHC integrated luminosity of $\mathcal{L} = 3000$ fb^{-1}. The MC samples used in the analysis are generated at particle-level and have not been run through the typical full simulation of the ATLAS detector Smearing functions derived from a `GEANT4` simulation of the upgraded ATLAS detector [24] are used to estimate detector effects such as momentum resolution. In addition, pileup events are fully simulated. The MC samples used in this analysis are summarized in Table 6.1.

The signal sample consists of both VBS and non-VBS electroweak (EWK) $W^\pm W^\pm jj$ production, and it is sumulated with the `Madgraph5_aMC@NLO` generator [32] using the `NNPDF3.0` PDF set [29] and
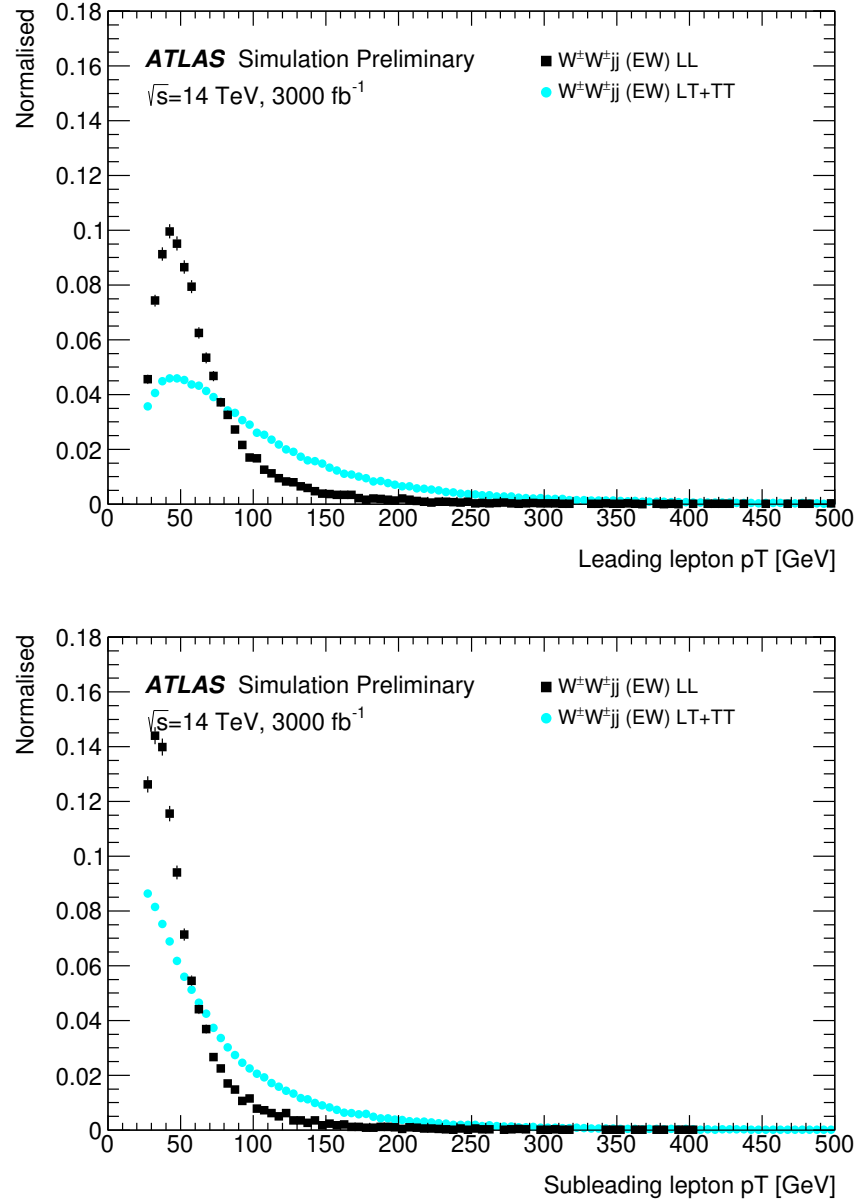
Figure 6.1: Comparison of the leading (top) and subleading (bottom) lepton p_T distributions for purely longitudinal (LL, black) and mixed polarization (LT+TT, cyan) $W^\pm W^\pm jj$ events. Plots from [3].
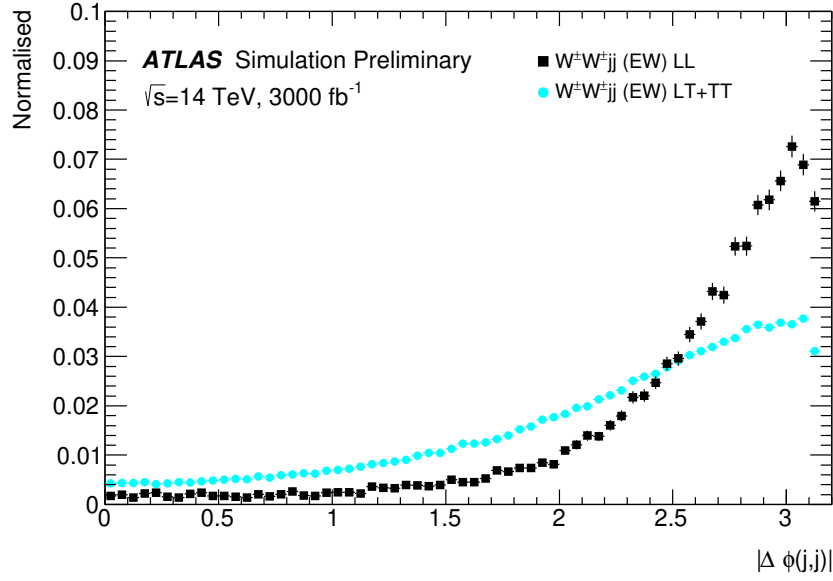
Figure 6.2: Comparison of the azimuthal dijet separation ($|\Delta\phi_{jj}|$) for purely longitudinal (LL, black) and mixed polarization (LT+TT, cyan) $W^{\pm}W^{\pm}jj$ events. Plot from [3].

interfaced with `PYTHIA v8` [51] for hadronization and parton showering. To study the longitudinal polarization more directly, two additional `Madgraph5_aMC@NLO` $W^{\pm}W^{\pm}jj$ samples are used: one containing only the longitudinal contribution (LL) and a second containing the transverse (TT) and mixed (LT) contributions.

There are many other processes that can produce the same final state as the $W^{\pm}W^{\pm}jj$ and must also be accounted for using MC simulations. WZ events are generated using `SHERPA v2.2.0` [26, 27, 28], which includes up to one parton at NLO in the strong coupling constant α_s and up to three additional partons at LO. Both EWK and QCD production are included in these samples. ZZ and triboson VVV ($V = W, Z$) events are generated using `SHERPA v2.2.2` with up to two additional partons in the final state. For the triboson backgrounds, the bosons can decay leptonically or hadronically. W+jets backgrounds are generated for electron, muon, and tau final states are generated at LO with `Madgraph5_aMC@NLO` and the `NNPDF3.0` set with showering from `PYTHIA v8`. Z+jets events are generated using `POWHEG-BOX v2` [30] and the `CT10` PDF set [33] interfaced with `PYTHIA v8`. Finally, $t\bar{t}$ and single-top events are generated using `POWHEG-BOX` with showering from `PYTHIA v6`.

Process	Generator	Comments
$W^\pm W^\pm jj$ (EWK)	`Madgraph5_aMC@NLO`	Signal sample
$W^\pm W^\pm jj$ (QCD)	`Madgraph5_aMC@NLO`	
$W^\pm W^\pm jj$ (LL)	`Madgraph5_aMC@NLO`	Pure longitudinal polarization sample
$W^\pm W^\pm jj$ (TT+LT)	`Madgraph5_aMC@NLO`	Mixed and transverse polarization sample
Diboson	`SHERPA v2.2.0`	WZ events
	`SHERPA v2.2.2`	ZZ events
Triboson	`SHERPA v2.2.2`	
W+jets	`Madgraph5_aMC@NLO`	
Z+jets	`POWHEG-BOX v2`	
$t\bar{t}$	`POWHEG-BOX`	
Single top	`POWHEG-BOS`	

Table 6.1: Summary of MC samples used in the analysis.

6.3 Background estimations

In this analysis, all background contributinos are estimated using MC simulations. Backgrounds such as electron charge misidentification and fake electrons from jets–which are traditionally estimated using data-driven techniques–are estimated using a set of parameterization functions applied to the MC. These functions calculate the probability that an electron is assigned the wrong charge or a jet is mis-reconstructed as an electron parameterized by the p_T and η of the electron or jet. The probabilites are derived from studies on expected electron performance with the upgraded ATLAS detector [52].

Processes involving two W and Z bosons are grouped together as *diboson* backgrounds, with the exception of $W^\pm W^\pm jj$ events produced via QCD interactions, which are kept separate. Similarly, all backgrounds with three vector bosons are combined and labeled as *triboson*. Any W+jets or top events that pass selection and do not contain a fake electron, as well as any Z+jets events without an electron identifed as having its charge misidentified are combined as *other non-prompt* backgrounds.

6.3.1 Truth-based isolation

Since the MC samples used in this analysis have not been run through a full detector simulation, they lack any kind of particle isolation variables (since they require, for example, information on the calorimeter response). Generally, this is not a large concern, as at truth-level, high p_T signal leptons tend to be well isolated to begin with. However, isolation is one of the most powerful tools for rejecting leptons from non-prompt sources such as top events, which are produced in association with additional nearby particles from b and c quark decays. In the absence of any sort of isolation

680 requirement, contributions from top backgrounds (including single top, $t\bar{t}$ and $t\bar{t} + V$) were more

681 than an order of magnitude higher than expected.

682 As a result, it was necessary to create an analogue to the isolation information that is available

683 in fully-simulated samples. Track- and calorimeter-based isolation variables were constructed by

684 summing the momentum and energy, respectively, of stable truth particles with $p_{\mathrm{T}} > 1$ GeV within a

685 specified radius of each signal lepton. For the track-based isolation, only charged truth particles were

686 used; both charged and neutral particles (excluding neutrinos) were included for the calorimeter-

687 based isolation. Ultimately, a set of isolation cuts were chosen that are similar to those recommended

688 by ATLAS for Run 2 analyses. The truth-based isolation requirements are listed in Table 6.2.

	Electron Isolation	Muon Isolation
Track-based isolation cone size	$\Delta R < 0.2$	$\Delta R < 0.3$
Track-based isolation requirement	$\sum p_{\mathrm{T}}/p_{\mathrm{T}}^e < 0.06$	$\sum p_{\mathrm{T}}/p_{\mathrm{T}}^\mu < 0.04$
Calorimeter-based isolation cone size	$\Delta R < 0.2$	$\Delta R < 0.2$
Calorimeter-based isolation requirement	$\sum E_{\mathrm{T}}/p_{\mathrm{T}}^e < 0.06$	$\sum E_{\mathrm{T}}/p_{\mathrm{T}}^\mu < 0.15$

Table 6.2: Truth-based isolation requirements for electrons and muons.

689 The truth-based isolation requirement reduced the top background by over 99% and reduced

690 the contribution of top events to the total background from 83% to 2%. Additional details on the

691 truth-based isolation studies are presented in Appendix A.

6.4 Object and event selection

6.4.1 Object selection

694 Electrons and muons are preselected to have $p_{\mathrm{T}} > 7$ and 6 GeV, respectively, and $|\eta| \leq 4.0$. The

695 likelihood of a given lepton to pass the trigger or identification requirements is estimated by estimat-

696 ing an efficiency dependent on the p_{T} and η of the lepton. The leptons are also required to pass the

697 isolation criteria detailed in Table 6.2. Jets that have been tagged as a fake electron by the functions

698 described earlier in Section 6.3 are treated as electrons for the purpose of the object selection and are

699 subject to the same criteria. In order to be considered a signal lepton, an additional requirement of

700 $p_{\mathrm{T}} > 25$ GeV is applied on top of the preselection. The two highest p_{T} leptons passing this selection

701 are chosen to be the leading and subleading signal leptons.

702 Jets are clustered using the anti-k_t algorithm [37] from final-state particles within a radius of

703 $\Delta R = 0.4$ (excluding muons and neutrinos). Jets are required to have $p_{\mathrm{T}} > 30$ GeV and lie within

704 $|\eta| < 4.5$, with an additional cut of $p_{\mathrm{T}} > 70$ GeV for jets above $|\eta| \geq 3.8$ in order to suppress

jets from pileup interactions. Jets overlapping with a preselected electron within $\Delta R_{e,j} < 0.05$ are removed in order to prevent double counting. The two highest p_T jets are defined as the leading and subleading *tag jets*.

6.4.2   Event selection

The default event selection is summarized in Table 6.3 and described here. Exactly two signal leptons are required with the same electric charge and separated from each other by 0.3 in ΔR. In order to suppress contributions from Drell-Yan backgrounds, the two signal leptons must have an invariant mass m_{ll} greater than 20 GeV. Additionally, if both signal leptons are electrons, their mass must be at least 10 GeV from the Z-boson mass in order to reduce background from Z-boson decays[4]. The event is required to have at least 40 GeV of missing transverse energy (E_T^{miss}) to account for the two neutrinos from the W decays. Events with additional preselected leptons are vetoed, which greatly reduces WZ and ZZ backgrounds. Both tag jets are required to not overlap with the signal leptons, and there is a veto on events with one or more b-jets. In order to preferentially select VBS production, the tag jets are also required to have a large separation between them and a large invariant mass. Finally, a cut on the lepton centrality, ζ, defined in Equation 6.1 enhances the EWK $W^{\pm}W^{\pm}jj$ signal.

$$\zeta = \min[\min(\eta_{\ell 1}, \eta_{\ell 2}) - \min(\eta_{j1}, \eta_{j2}), \max(\eta_{j1}, \eta_{j2}) - \max(\eta_{\ell 1}, \eta_{\ell 2})] \tag{6.1}$$

6.5   Selection optimization

As mentioned earlier, the HL-LHC will feature forward tracking, an increase in center of mass energy, and a higher integrated luminosity. Therefore, this study is an excellent time to see if there are new optimizations to the signal event selection that can improve the signal to background ratio.

6.5.1   Random grid search algorithm

The chosen method for optimizing the event selection is a cut-based algorithm known as the Random Grid Search (RGS) [53]. Consider a simple case of two variables x and y chosen to differentiate the signal from the background. In order to be considered a signal event, a given event would be required to pass a *cut point* $c = \{x > x_c, y > y_c\}$. A simple method to choose the optimal cut point (i.e. the

---

[4]The electron charge mis-ID rate is high enough that contributions from $Z \to ee$ backgrounds are non-negligible.

Selection requirement	Selection value
Lepton kinematics	$p_\mathrm{T} > 25$ GeV
	$\lvert\eta\rvert \leq 4.0$
Jet kinematics	$p_\mathrm{T} > 30$ GeV for $\lvert\eta\rvert \leq 4.5$
	$p_\mathrm{T} > 70$ GeV for $\lvert\eta\rvert > 3.8$
Dilepton charge	Exactly two signal leptons with same charge
Dilepton separation	$\Delta R_{l,l} \geq 0.3$
Dilepton mass	$m_{ll} > 20$ GeV
Z boson veto	$\lvert m_{ee} - m_Z\rvert > 10$ GeV (ee-channel only)
$E_\mathrm{T}^\mathrm{miss}$	$E_\mathrm{T}^\mathrm{miss} > 40$ GeV
Jet selection	At least two jets with $\Delta R_{l,j} > 0.3$
b jet veto	$N_\mathrm{b\text{-}jet} = 0$
Dijet separation	$\Delta\eta_{jj} > 2.5$
Trilepton veto	No additional preselected leptons
Dijet mass	$m_{jj} > 500$ GeV
Lepton-jet centrality	$\zeta > 0$

Table 6.3: Summary of the signal event selection.

"best" values of the cuts x_c and y_c) would be to construct an $n \times m$ rectangular grid in x and y consisting of points $(x_0, y_0), (x_1, y_1), ..., (x_n, y_m)$, as in Figure 6.3. One can then choose a cut point $c_k = \{x > x_i, y > y_j\}$ that maximizes the signal significance as measured by a chosen metric. This would be considered a *regular* or *rectangular* grid search.

While effective in principle, this rectangular grid search comes with two major drawbacks:

1. The algorithm does not scale well as the number of variables to be optimized–the dimensionality of the grid–increases. In the case of a square grid with N bins per variable v, the number of cut points to be evaluated grows as N^v.

2. Signal and background samples are rarely evenly distributed over the entire grid, resulting in many cut points being sub-optimal and evaluating them would be a waste of computing resources.

To combat these limitations, the RGS algorithm constructs a grid of cut points directly from the signal sample itself. In the two-dimensional example, this means that the variables x_i and y_j making up the cut point $c_k = \{x > x_i, y > y_j\}$ take their values directly from a given signal event. This has the benefit of creating a *random grid* of cut points that is by construction biased towards regions of high signal concentration. This reduces the need for exponentially increasing numbers of cut points while ensuring that computing resources are not wasted in regions with few to no signal events. An example of the the two-dimensional random grid is shown in Figure 6.4.
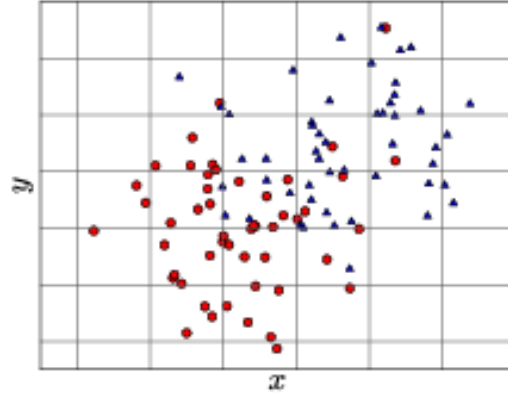
Figure 6.3: A visual representation of a rectangular grid search algorithm. The signal events are the blue triangles, and the red circles are the background events. TODO: replace with own figure
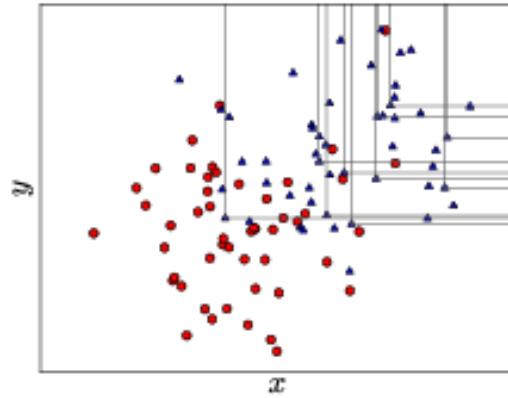
Figure 6.4: A visual representation of a random grid search algorithm. The signal events are the blue triangles, and the red circles are the background events. TODO: replace with own figure

748   Once the random grid of cut points is constructed, the optimal cut point can be chosen using

749   whatever metric the analyzer chooses, such as signal to background ratio. For the purpose of the

750   $W^{\pm}W^{\pm}jj$ upgrade study, the optimal cut point is the one that mazimizes the signal significance Z

751   defined as in Equation 6.2 [54].

$$Z = \sqrt{2\left[(s+b)\ln\left(\frac{s+b}{b_0}\right) + b_0 - s - b\right] + \frac{(b-b_0)^2}{\sigma_b^2}} \tag{6.2}$$

752   where s and b are the number of signal and background events, respectively, σ_b is the total uncertainty

753   on the background, and b_0 is defined as:

$$b_0 = \frac{1}{2}\left(b - \sigma_b^2 + \sqrt{(b - \sigma_b^2)^2 + 4(s+b)\sigma_b^2}\right) \tag{6.3}$$

754   In the case where the backround is known precisely (i.e. $\sigma_b = 0$), Equation 6.2 simplifies to

$$Z = \sqrt{2\left(b\big[(1 + s/b)\ln(1 + s/b) - s/b\big]\right)} \tag{6.4}$$

755   which further reduces to the familiar $Z = s/\sqrt{b}$ for the case when $s << b$.

6.5.2   Inputs to the optimization

757   In order to train the RGS, signal and background samples were prepared from events passing the

758   event selection outlined in Table 6.3 up through the b-jet veto. The signal sample was chosen to

759   be the longitudinally polarized $W^{\pm}W^{\pm}jj$ EWK events, and the transverse and mixed polarizations

760   were treated as background along with $W^{\pm}W^{\pm}jj$ events from QCD interactions and the traditional

761   backgrounds listed in Section 6.3. Splitting the inclusive $W^{\pm}W^{\pm}jj$ EWK events by polarization

762   allows the optimization to favor the longitunally polarized events as much as possible, even though

763   they both contribute to the EWK signal.

764   The following variables were chosen for optimization:

765   • Leading lepton p_{T}

766   • Dilepton invariant mass (m_{ll})

767   • Leading and subleading jet p_{T}

768   • Dijet invariant mass (m_{jj})

769   • Lepton-jet centrality (ζ)

770 Subleading lepton p_{T} was omitted as it is desirable to keep the cut value as low as possible due to
771 its sensitivity to the longitudinal polarization (as discussed in Section 6.1.1). Additionally, the dijet
772 separation $\Delta\eta_{jj}$ was included in the optimization originally, however it was dropped from the list due
773 to the cut value being motivated by differences between EWK and QCD produced $W^{\pm}W^{\pm}jj$ events.

774   Two additional constraints were imposed when selecting the optimal cut point:

775 1. At least 1000 signal events must survive in order to prevent the optimization from being too
776   aggressive and unnecssarily reducing signal statistics.

777 2. The dijet invariant mass may only vary within a 50 GeV range of the default value (from
778     $450 - 550$ GeV) due to the cut being physically motivated by the VBS event topology (TODO:
779   reference where this is discussed in the 13 TeV section).

780   Lastly, the decision was made to use calculate the signal significance without taking into account
781 the uncertainty of the background using Equation 6.4. This was due to the fact that the statistical
782 uncertainties of the fake electron and charge-misID backgrounds were quite large, and if Equation 6.2
783 were used instead, the optimization would cut unreasonably hard against these backgrounds. Since
784 Monte Carlo statistics is not expected to be a limiting factor when this analysis is performed at the
785 HL-LHC, it is more realistic to simply ignore these large statistical uncertainties for the purpose of
786 the selection optimization.

787 ### 6.5.3   Results of the optimization

788 Ultimately, the random grid was constructed from over 38,000 LL-polarized $W^{\pm}W^{\pm}jj$ events in
789 the variables listed above. After applying the constraints, an optimal cut point was chosen which
790 reduced the total background from 9900 to 2310 while reducing the signal from 3489 to 2958. This
791 corresponds to an increase in signal significance from $Z = 33.26$ to $Z = 52.63$ as calculated by
792 Equation 6.4. The updates to the event selection are listed in Table 6.4.

793   The large reduction in the background is primarily a result of the increase in the leading and
794 subleading jet p_{T} from 30 GeV to 90 GeV and 45 GeV, respectively. As can be seen in Figure 6.7,
795 this increase removes a significant portion of the backgrounds from jets faking electrons and charge
796 mis-ID. Additionally, the loosening of the lepton-jet centrality cut ζ allows more signal events to
797 survive the event selection (see Figure 6.9). Other changes to the event selection are minor and do
798 not individually have a large impact on the signal or background yields.

The full event yields after optimization as well as the cross section measurement are detailed alongside those using the default selection in Section 6.6.

TODO: It's a bit awkward to reference the results of the default/optimized before they're properly presented. Maybe move the sections around? not sure...

Selection requirement	Selection value
Lepton kinematics	$p_\mathrm{T} > 28$ GeV (leading lepton only)
Jet kinematics	$p_\mathrm{T} > 90$ GeV (leading jet) $p_\mathrm{T} > 45$ GeV (subleading jet)
Dilepton mass	$m_{ll} > 28$ GeV
Dijet mass	$m_{jj} > 520$ GeV
Lepton-jet centrality	$\zeta > -0.5$

Table 6.4: Updates to the $W^{\pm}W^{\pm}jj$ event selection criteria after optimization. Cuts not listed remain unchanged from the default selection in Table 6.3.

Figure 6.5: Leading lepton p_T distribution. The default and optimized cuts are represented by the red and green dashed lines, respectively. The $W^{\pm}W^{\pm}jj$ EWK signal (black points) is normalized to the same area as the sum of the backgrounds (colored histogram). TODO: Move to appendix or omit

Figure 6.6: Dilepton invariant mass distribution. The default and optimized cuts are represented by the red and green dashed lines, respectively. The $W^{\pm}W^{\pm}jj$ EWK signal (black points) is normalized to the same area as the sum of the backgrounds (colored histogram). TODO: Move to appendix or omit

6.6 Results

6.6.1 Event yields

After applying the full event selection, the analysis is broken down into four channels based off of the flavor of the signal leptons: $\mu\mu$, ee, μe, and $e\mu$. The full signal and background event yields are shown in Table 6.5 for each channel separately and combined using the default event selection. 3489 EWK $W^{\pm}W^{\pm}jj$ events are expected compared to 9900 background events. The dominant sources of background are jets faking electrons followed by charge misidentification and diboson processes. Triboson events, QCD $W^{\pm}W^{\pm}jj$, and other non-prompt sources make up approximately 5% of the total background combined.

The event yields for the optimized selection detailed in Section 6.5.3 are listed in Table 6.6. After optimization, 2958 signal events and just 2310 background events are expected. Diboson events now are the primary source of background, as the optimization greatly reduces the fake and charge misidentification backgrounds. As discussed earlier, the increase in the leading and subleading jet p_{T} cuts as well as the loosening of the centrality cut are most responsible for the changes in the signal and background yields; distributions of these quantities using the default and the optimized
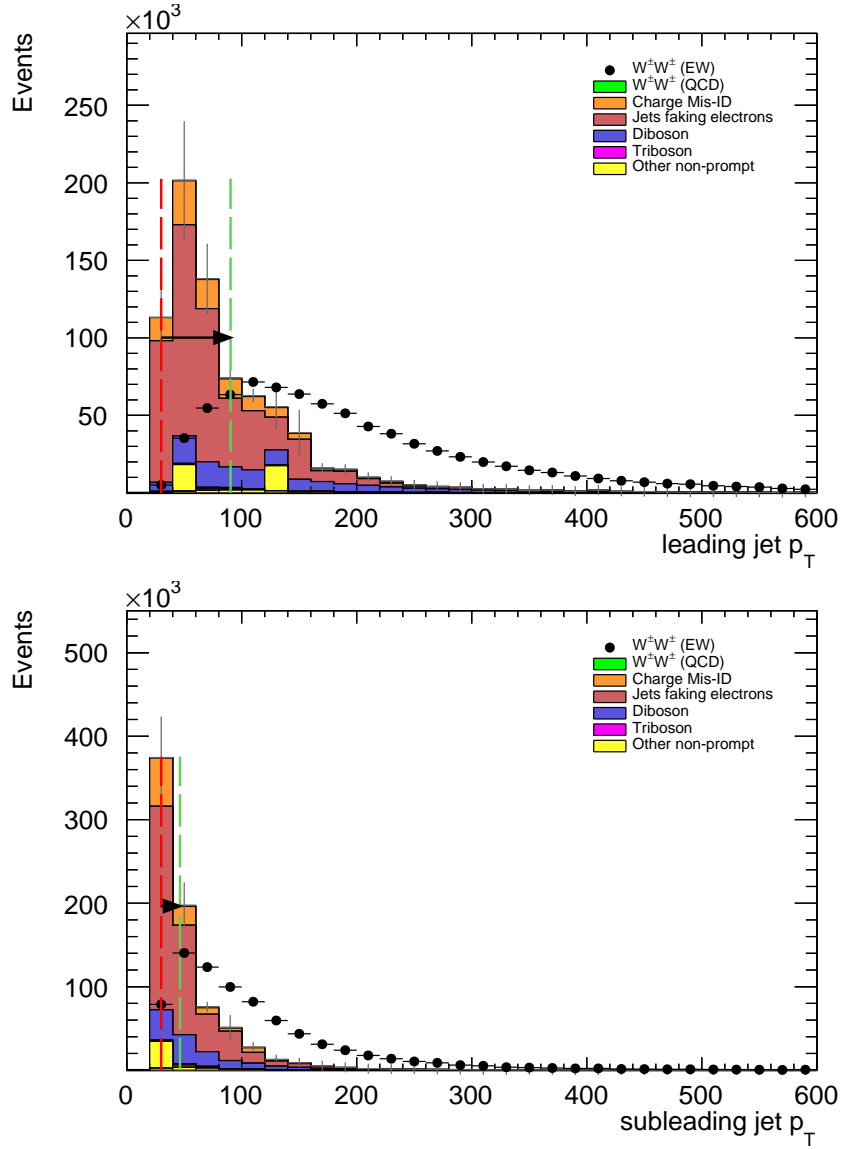
Figure 6.7: Leading (top) and subleading (bottom) jet p_T distributions. The default and optimized cuts are represented by the red and green dashed lines, respectively. The $W^{\pm}W^{\pm}jj$ EWK signal (black points) is normalized to the same area as the sum of the backgrounds (colored histogram).
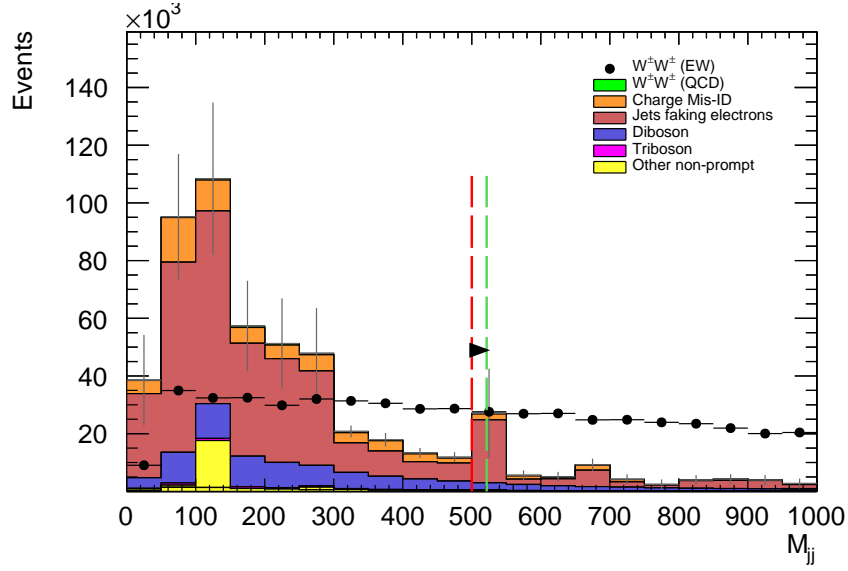
Figure 6.8: Dijet invariant mass distribution. The default and optimized cuts are represented by the red and green dashed lines, respectively. The $W^{\pm}W^{\pm}jj$ EWK signal (black points) is normalized to the same area as the sum of the backgrounds (colored histogram). TODO: Move to appendix or omit
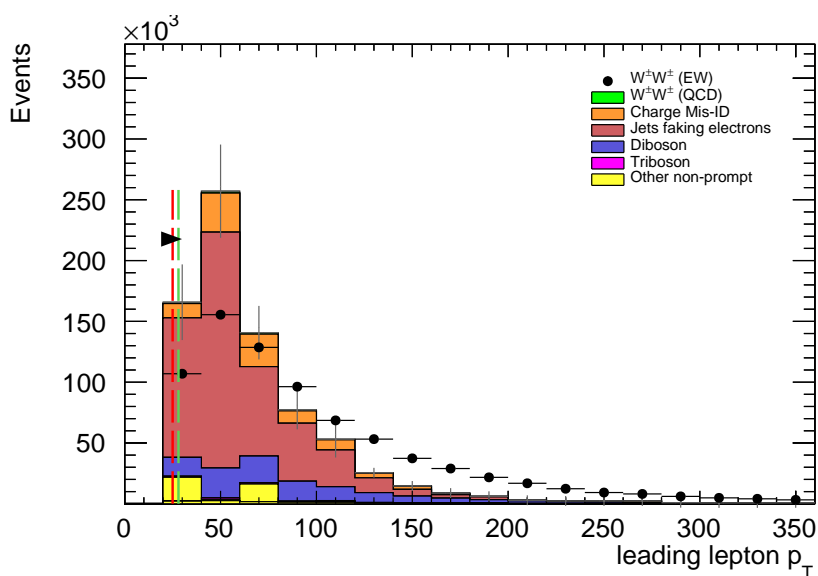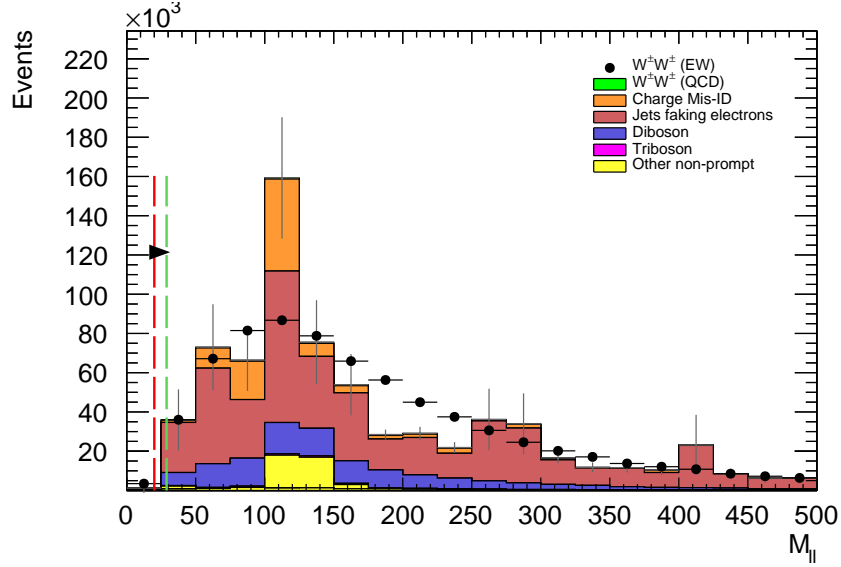

Figure 6.9: Lepton-jet centrality distribution. The default and optimized cuts are represented by the red and green dashed lines, respectively. The $W^{\pm}W^{\pm}jj$ EWK signal (black points) is normalized to the same area as the sum of the backgrounds (colored histogram).
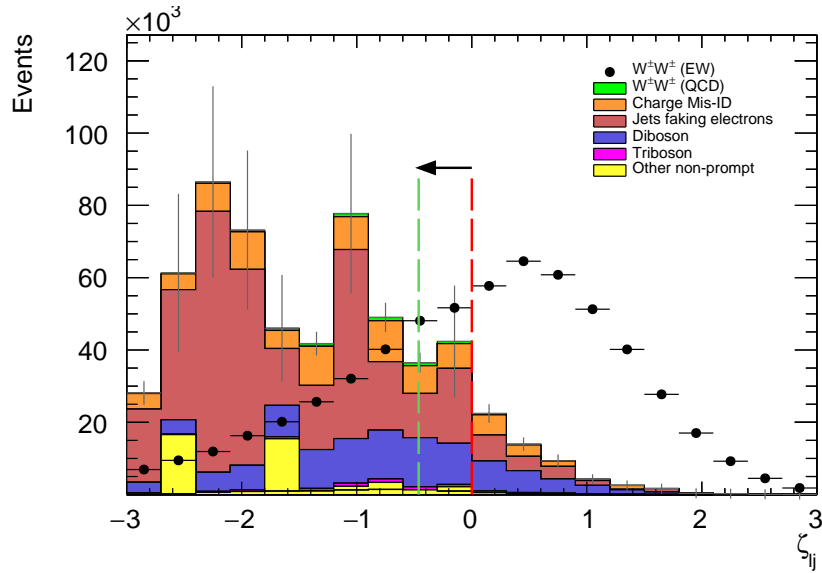
	All channels	$\mu\mu$	ee	μe	$e\mu$
$W^{\pm}W^{\pm}jj$ (QCD)	206.4	91.1	22.8	38.4	54.1
Charge Misidentification	2300	0.0	2100	90	160
Jets faking electrons	5000	0.0	3400	1200	340
$WZ + ZZ$	2040	500	438	423	680
Tribosons	115	47	15.4	21.6	31.2
Other non-prompt	210	110	20	60	27
Total Background	9900	750	6000	1900	1290
Signal $W^{\pm}W^{\pm}jj$ (EWK)	3489	1435	432	679	944

Table 6.5: Signal and background event yields using the default event selection for an integrated luminosity of $\mathcal{L} = 3000$ fb^{-1}. Events containing a fake or charge-flipped electron are removed from their respective sources and combined into a single entry each.

event selections can be found in Figures 6.10, 6.11, and 6.12, respectively.

	All channels	$\mu\mu$	ee	μe	$e\mu$
$W^{\pm}W^{\pm}jj$ (QCD)	168.7	74.6	19.7	32.2	42.2
Charge Misidentification	200	0.0	11	30	160
Jets faking electrons	460	0.0	130	260	70
$WZ + ZZ$	1286	322	289	271	404
Tribosons	76	30.1	9.6	15.1	21.6
Other non-prompt	120	29	16.6	50	19
Total Background	2310	455	480	660	710
Signal $W^{\pm}W^{\pm}jj$ (EWK)	2958	1228	380	589	761

Table 6.6: Signal and background event yields using the optimized event selection for an integrated luminosity of $\mathcal{L} = 3000$ fb^{-1}. Events containing a fake or charge-flipped electron are removed from their respective sources and combined into a single entry each.

It is important to note, however, that the MC sample used to estimate Z+jets events suffers from poor statistics which results in large per-event weights once scaled to $\mathcal{L} = 3000$ fb^{-1}. This sample contributes heavily to the fake and charge misidentification backgrounds, and a handful of these events being cut out by the optimization contributes has a large effect on the dramatic reduction of these backgrounds. As a result, these particular optimized results are likely overly optimistic. However, given proper MC statistics, it is still expected that the optimization will outperform the default selection.

6.6.2 Uncertainties

TODO: Ask for details on how some of these uncertainties were calculated – specifically the fakes and charge mis-ID The uncertainties considered for the analysis are summarized in Table 6.7. Values for experimental systematics on the trigger efficiency, lepton and jet reconstruction, and flavor tagging

Figure 6.10: p_T distributions for the leading jet using the default (left) and optimized (right) event selections for all channels combined.
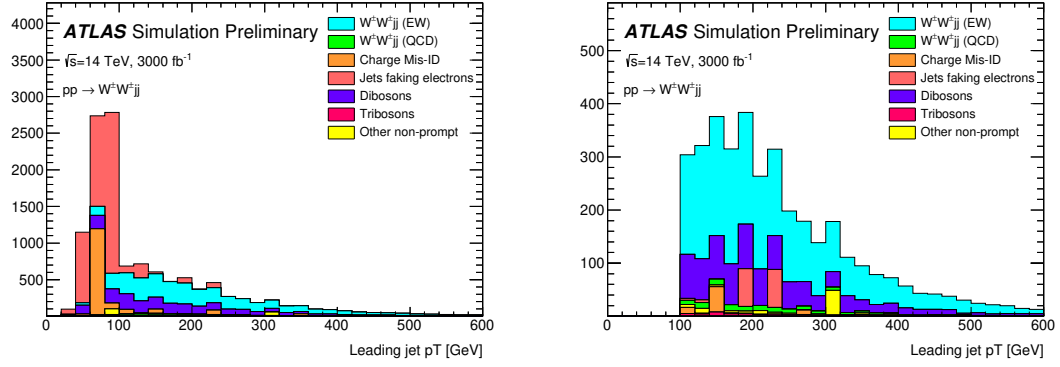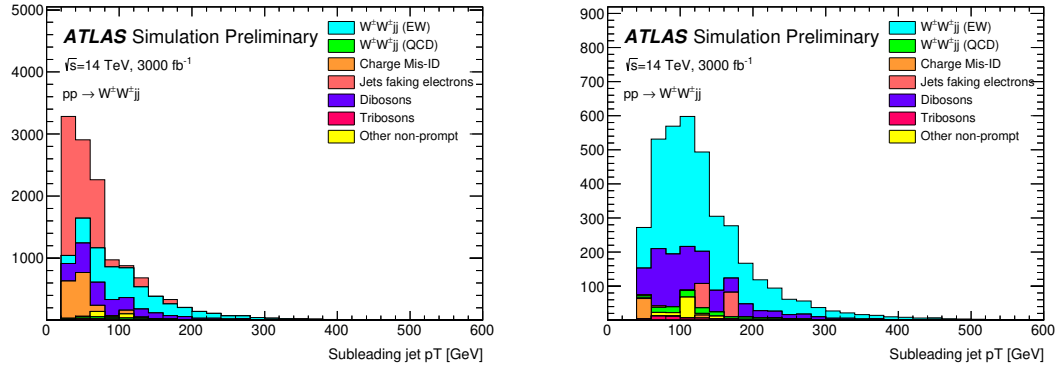

Figure 6.11: p_T distributions for the subleading jet using the default (left) and optimized (right) event selections for all channels combined.
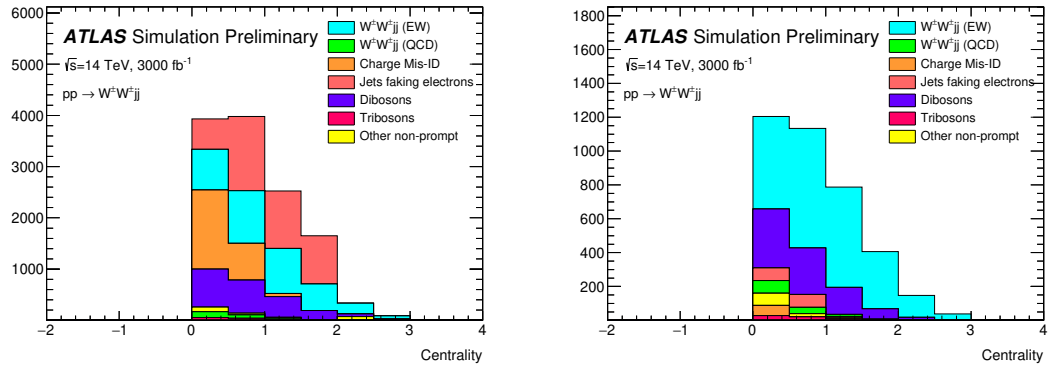

Figure 6.12: p_T distributions for lepton-jet centrality ζ using the default (left) and optimized (right) event selections for all channels combined.

are taken directly from the 13 TeV analysis TODO: (cite or reference?). The rate uncertainties for the background processes are halved from the 13 TeV values.

Source	Uncertainty (%)
$W^\pm W^\pm jj$ (EWK)	3
Luminosity	1
Trigger efficiency	0.5
Lepton reconstruction and identification	1.8
Jets	2.3
Flavor tagging	1.8
Jets faking electrons	20
Charge misidentification	25
$W^\pm W^\pm jj$ (QCD)	20
Top	15
Diboson	10
Triboson	15

Table 6.7: Summary of estimated experimental and rate uncertainties.

6.6.3   Cross section measurement

The cross section is calculated using the same method as in the 13 TeV analysis, detailed in Chapter 5. TODO: update from chapter reference to subsection reference (once it's written)... Once again, each of the four lepton flavor channels is further split by charge (i.e. $\mu\mu \to \mu^+\mu^+ + \mu^-\mu^-$), as this increases the sensitivity of the analysis. Each channel's m_{jj} distribution is combined in a profile likelihood fit to extract the EWK $W^\pm W^\pm jj$ production cross section. The expected cross section calculated using the default event selection is:

$$\sigma^{\text{expected}}_{W^\pm W^\pm jj} = 16.89 \pm 0.36 \ (\text{stat}) \pm 0.53 \ (\text{theory}) \pm 0.84 \ (\text{syst}) \ \text{fb} \qquad (6.5)$$

The expected cross section calculated using the optimized event selection is:

$$\sigma^{\text{expected}}_{W^\pm W^\pm jj} = 16.94 \pm 0.36 \ (\text{stat}) \pm 0.53 \ (\text{theory}) \pm 0.78 \ (\text{syst}) \ \text{fb} \qquad (6.6)$$

The optimized selection should not change the measured value of the cross section, and indeed both are consistent with within uncertainties. The sytematic uncertainty is reduced by approximately 7% with the optimized selection. Projections of the total uncertainty on the cross section as a function of integrated luminosity made by TODO: how was this made? is shown in Figure 6.13.

6.6.4   Longitudinal scattering significance
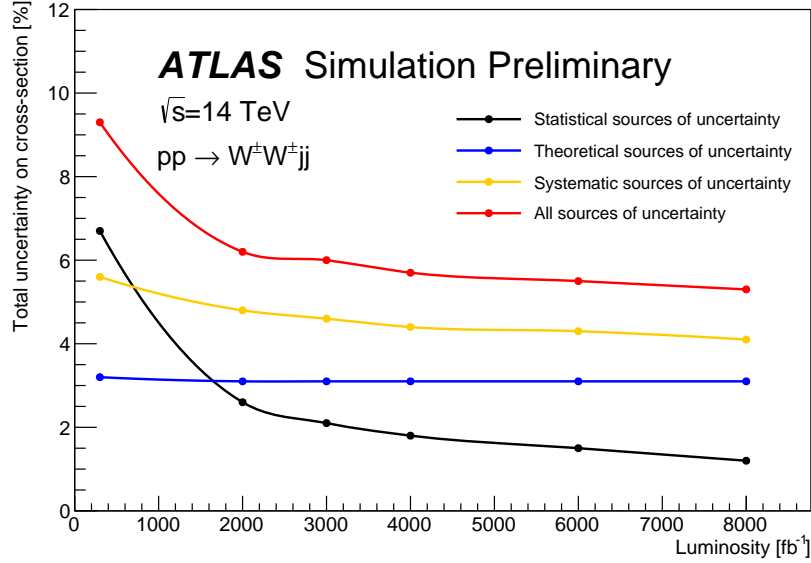
Figure 6.13: Projections of the statistical (black), theoretical (blue), systematic (yellow), and total (red) uncertainties on the measured cross section as a function of integrated luminosity using the optimized event selection.

TODO: get some details on how this was all done... The longitudinal scattering significance is extracted from the $|\Delta\phi_{jj}|$ distribution using a simultaneous binned likelihood fit. In order to increase sensitivity, the $|\Delta\phi_{jj}|$ distribution was split into two bins in m_{jj}, and an additional cut on the pseudorapidity of the subleading lepton was applied ($|\eta| < 2.5$) to reduce background from fake and charge misidentification. The $|\Delta\phi_{jj}|$ distributions used in the fit are shown in Figure 6.14. Due to limited statistics, the four lepton flavor channels were not split by charge. The expected significance of the $W_L^{\pm}W_L^{\pm}jj$ process is 1.8σ with a precision of 47% on the measurement. Projections of the expected significance as a function of integrated luminosity is shown in Figure 6.15.
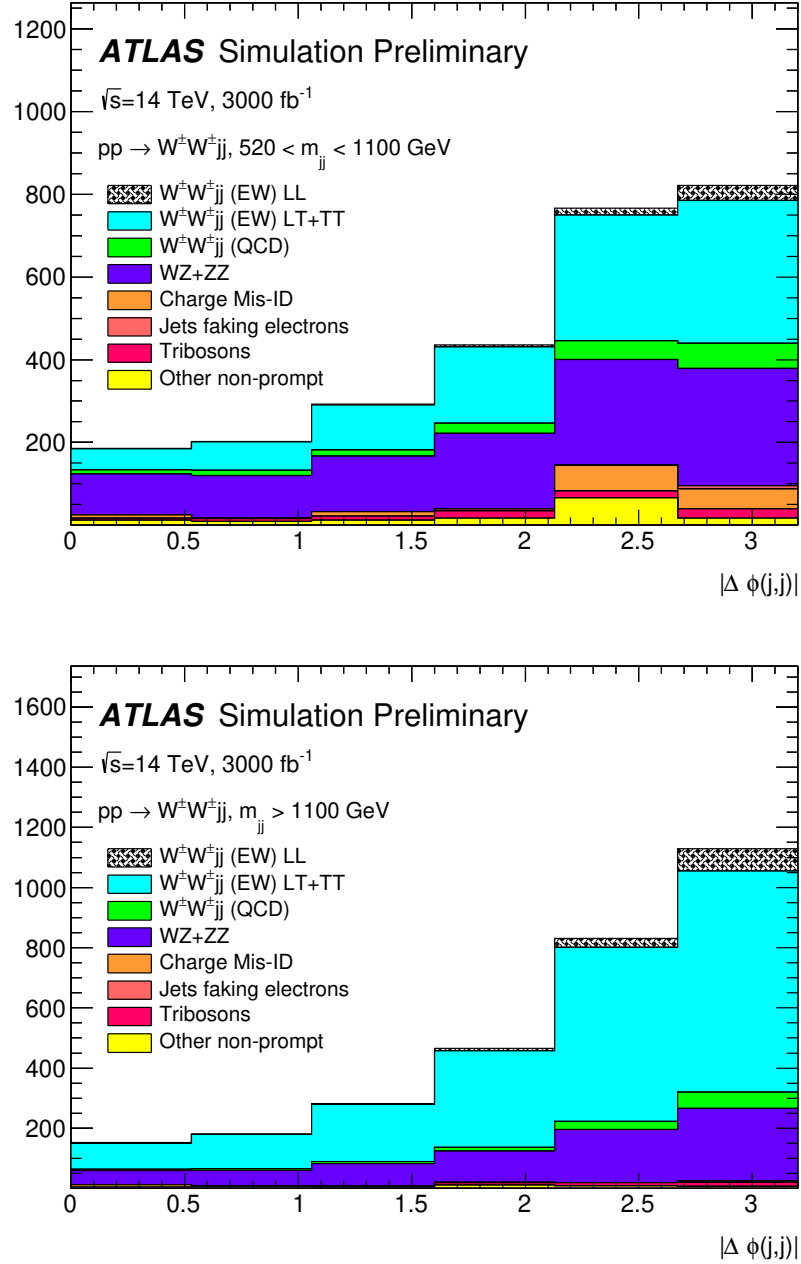
Figure 6.14: Dijet azimuthal separation ($|\Delta\phi_{jj}|$) for the low m_{jj} region ($520 < m_{jj} < 1100$ GeV, top) and the high m_{jj} region ($m_{jj} > 1100$ GeV, bottom). The purely longitudinal (LL, gray) is plotted separately from the mixed and transverse (LT+TT, cyan) polarizations.
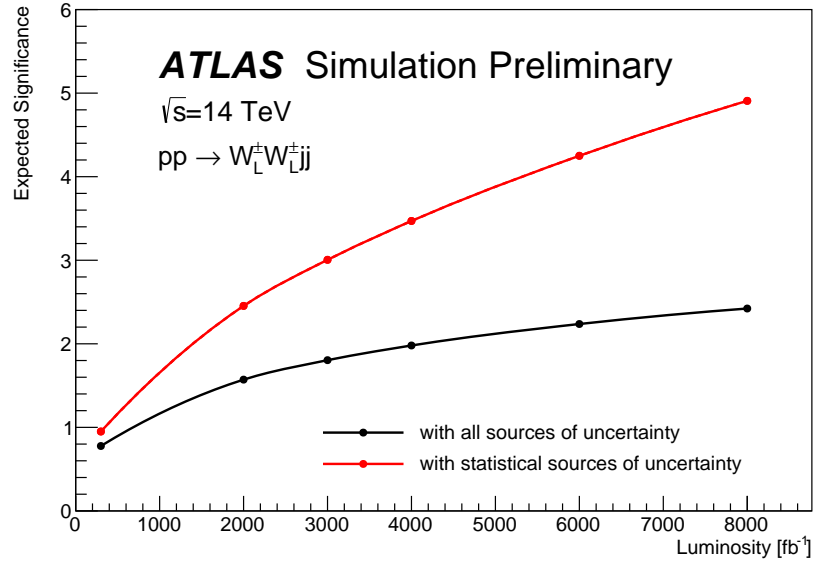
Figure 6.15: Projections of the expected longitudinal scattering significance as a function of integrated luminosity when considering all sources of uncertainties (black) or only statistical uncertainties (red).

CHAPTER 7

Conclusion

Here's where you wrap it up.

Looking Ahead

Here's an example of how to have an "informal subsection".

Appendix A

Additional material on truth isolation

yields by type	all channels	$\mu\mu$	ee	μe	$e\mu$
signal	4011	1583.2	531.7	793.1	1103.1
ww qcd	252.6	105.8	30.4	48	68.4
charge flip	2528.4	0.0	2075.4	255.1	197.8
fakes	7135.4	0.0	4675.1	1904.3	555.9
diboson	2370.4	581.2	491.8	517.9	779.6
triboson	125.5	49.1	17.8	24.6	34.1
top	90150.5	26618	15301.6	25277.9	22953.1
z+jets	241.2	0.0	0.0	0.0	241.2
w+jets	31.4	3.9	7.6	13.2	6.7
total bkg	102803.9	27354	22592	28027.8	24830.1
signal	4011	1583.2	531.7	793.1	1103.1

Table A.1: Event yields prior to applying any form of truth-based isolation criteria.

yields by type	all channels	$\mu\mu$	ee	μe	$e\mu$
signal	3470.5	1427.3	428.8	675.8	938.7
ww qcd	205.8	90.8	22.7	38.3	54
charge flip	2398.3	0.0	2104.6	95.8	197.9
fakes	4309.7	0.0	3390.6	750.8	168.3
diboson	1552.4	311.3	355.6	346.8	538.7
triboson	115	46.8	15.4	21.6	31.2
top	156.9	42.3	14.8	76.6	23.3
z+jets	0.0	0.0	0.0	0.0	0.0
w+jets	0.3	0.0	0.0	0.3	0.0
total bkg	8738.1	491.3	5903.7	1329.8	1013.4
signal	3470.5	1427.3	428.8	675.8	938.7

Table A.2: Event yields after applying a test version of the truth-based isolation.

TODO: Add tables for tight vs loose working point, information on the necessity of TRUTH1++

Bibliography

[1] P. Anger, B. Axen, T. Dai, C. Gumpert, C. Hasterok, B. Heinemann, M. Hurwitz, N. Ilic, M. Kobel, J. Liu, L. Liu, J. Metcalfe, S. Pagan Griso, B. Zhou, S. Hou, M.-A. Pleier, U. Schnoor, J. Searcy, F. Socher, A. Sood, A. Vest, L. Xu, and J. Zhu, *Same Sign $W^{\pm}W^{\pm}$ Production and Limits on Anomalous Quartic Gauge Couplings*, Tech. Rep. ATL-COM-PHYS-2013-990, CERN, Geneva, Jul, 2013. https://cds.cern.ch/record/1561731. Internal note for approved paper STDM-2013-06 https://atlas.web.cern.ch/Atlas/GROUPS/PHYSICS/PAPERS/STDM-2013-06/. (document), 5.1

[2] A. Alboteanu, W. Kilian, and J. Reuter, *Resonances and Unitarity in Weak Boson Scattering at the LHC*, JHEP **1**1 (2008) 010, arXiv:0806.4145 [hep-ph]. (document), 5.0.1, 5.1

[3] K. J. Potamianos, W. K. Di Clemente, M.-A. Pleier, C. A. Lee, J. I. Kroll, S. Yacoob, and M. Leigh, *Prospects for the measurement of the $W^{\pm}W^{\pm}$ scattering cross section and extraction of the longitudinal scattering component in pp collisions at the High-Luminosity LHC with the ATLAS experiment.*, Tech. Rep. ATL-COM-PHYS-2018-1479, CERN, Geneva, Oct, 2018. https://cds.cern.ch/record/2644264. (document), 6.1, 6.2

[4] S. L. Glashow, *The Renormalizability of Vector Meson Interactions*, Nucl. Phys. **10** (1959) 107–117. 2.2

[5] A. Salam and J. C. Ward, *Weak and Electromagnetic Interactions*, Nuovo Cimento **11** (1959) 568–577. 2.2

[6] L. R. Evans and P. Bryant, *LHC Machine*, JINST **3** (2008) S08001. https://cds.cern.ch/record/1129806. This report is an abridged version of the LHC Design Report (CERN-2004-003). 3.1

[7] ATLAS Collaboration, *The ATLAS Experiment at the CERN Large Hadron Collider*, JINST **3** (2008) S08003. 3.1

[8] ATLAS Collaboration Collaboration, *Alignment of the ATLAS Inner Detector Tracking System with 2010 LHC proton-proton collisions at $\sqrt{s} = 7\ TeV$*, Tech. Rep. ATLAS-CONF-2011-012, CERN, Geneva, Mar, 2011. https://cds.cern.ch/record/1334582. 4

891 [9] ATLAS Collaboration, ATLAS Collaboration, *Evidence for Electroweak Production*
892   *of $W^{\pm}W^{\pm}jj$ in pp Collisions at $\sqrt{s} = 8$ TeV with the ATLAS Detector*, Phys. Rev. Lett. **113**
893   (2014) no. 14, 141803, arXiv:1405.6241 [hep-ex]. 5

894 [10] CMS Collaboration, V. Khachatryan et al., *Study of vector boson scattering and search for*
895   *new physics in events with two same-sign leptons and two jets*, Phys. Rev. Lett. **1**14 (2015)
896   no. 5, 051801, arXiv:1410.6315 [hep-ex]. 5

897 [11] ATLAS Collaboration Collaboration, *Observation of electroweak production of a same-sign W*
898   *boson pair in association with two jets in pp collisions at $\sqrt{s} = 13$ TeV with the ATLAS*
899   *detector*, Tech. Rep. ATLAS-CONF-2018-030, CERN, Geneva, Jul, 2018.
900   https://cds.cern.ch/record/2629411. 5

901 [12] CMS Collaboration, CMS Collaboration, *Observation of electroweak production of same-sign*
902   *W boson pairs in the two jet and two same-sign lepton final state in proton-proton collisions*
903   *at $\sqrt{s} = 13$ TeV*, arXiv:1709.05822 [hep-ex]. 5

904 [13] C. Bittrich, W. K. Di Clemente, E. M. Duffield, C. Geng, G. Gonella, J. Guo, B. Heinemann,
905   T. Herrmann, F. Iltzsche Speiser, M. Kobel, K. Koeneke, J. I. Kroll, S. Li, J. Liu, Y. Liu, J. A.
906   Manjarres Ramos, G. Azuelos, C. A. Lee, M. Mittal, C. Mwewa, R. Ospanov, S. Pagan Griso,
907   K. J. Potamianos, M. Shapiro, P. Sommer, S. Todt, Y. Wu, W. Xu, S. Yacoob, H. Yang,
908   L. Zhang, Z. Zhao, B. Zhou, J. Zhu, and M.-A. Pleier, *Support note for measurement of*
909   *electroweak $W^{\pm}W^{\pm}jj$ production at $\sqrt{s} = 13$ TeV*, Tech. Rep. ATL-COM-PHYS-2018-252,
910   CERN, Geneva, Mar, 2018. https://cds.cern.ch/record/2309552. 5

911 [14] B. W. Lee, C. Quigg, and H. B. Thacker, *The Strength of Weak Interactions at Very*
912   *High-Energies and the Higgs Boson Mass*, Phys. Rev. Lett. **3**8 (1977) 883–885. 5.0.1, 6.1

913 [15] S. D. Rindani, *Strong gauge boson scattering at the LHC*, in *Physics at the Large Hadron*
914   *Collider*, A. Datta, B. Mukhopadhyaya, A. Raychaudhuri, A. K. Gupta, C. L. Khetrapal,
915   T. Padmanabhan, and M. Vijayan, eds., pp. 145–155. 2009. arXiv:0910.5068 [hep-ph]. 5.0.1

916 [16] ATLAS Collaboration, *Observation of a new particle in the search for the Standard Model*
917   *Higgs boson with the ATLAS detector at the LHC*, Phys. Lett. B **7**16 (2012) 1,
918   arXiv:1207.7214 [hep-ex]. 5.0.1

919 [17] CMS Collaboration, *Observation of a new boson at a mass of 125 GeV with the CMS*
920   *experiment at the LHC*, Phys. Lett. B **7**16 (2012) 30, arXiv:1207.7235 [hep-ex]. 5.0.1

921 [18] J. M. Campbell and R. K. Ellis, *Higgs Constraints from Vector Boson Fusion and Scattering*,
922   JHEP **0**4 (2015) 030, arXiv:1502.02990 [hep-ph]. 5.0.1

923 [19] M. SZleper, *The Higgs boson and the physics of WW scattering before and after Higgs*
924   *discovery*, arXiv:1412.8367 [hep-ph]. 5.0.1

925 [20] E. Accomando, A. Ballestrero, A. Belhouari, and E. Maina, *Isolating vector boson scattering*
926   *at the CERN LHC: Gauge cancellations and the equivalent vector boson approximation versus*
927   *complete calculations*, Phys. Rev. D **7**4 (Oct, 2006) 073010.
928   https://link.aps.org/doi/10.1103/PhysRevD.74.073010. 5.0.1

929 [21] ATLAS Collaboration, M. Aaboud et al., *Luminosity determination in pp collisions at $\sqrt{s} =$*
930   *8 TeV using the ATLAS detector at the LHC*, Eur. Phys. J. **C**76 (2016) no. 12, 653,
931   arXiv:1608.03953 [hep-ex]. 5.1

[22] G. Avoni et al., *The new LUCID-2 detector for luminosity measurement and monitoring in ATLAS*, JINST **13** (2018) no. 07, P07017. 5.1

[23] ATLAS Collaboration, G. Aad et al., *The ATLAS Simulation Infrastructure*, Eur. Phys. J. **C70** (2010) 823–874, arXiv:1005.4568 [physics.ins-det]. 5.1.1

[24] S. Agostinelli et al., *GEANT4 - a simulation toolkit*, Nucl. Instrum. Meth. **A506** (2003) 250–303. 5.1.1, 6.2

[25] T. Sjostrand, S. Mrenna, and P. Skands, *A Brief Introduction to PYTHIA 8.1*, Comput. Phys. Commun. **1**78 (2008) 852–867, arXiv:0710.3820 [hep-ph]. 5.1.1

[26] T. Gleisberg et al., *Event generation with SHERPA 1.1*, JHEP **0**2 (2009) 007, arXiv:0811.4622 [hep-ph]. 5.1.1, 6.2

[27] S. Schumann and F. Krauss, *A parton shower algorithm based on Catani-Seymour dipole factorization*, JHEP **0**3 (2008) 038, arXiv:0709.1027 [hep-ph]. 5.1.1, 6.2

[28] S. Höche, F. Krauss, S. Schumann, and F. Siegert, *QCD matrix elements and truncated showers*, JHEP **0**5 (2009) 053, arXiv:0903.1219 [hep-ph]. 5.1.1, 6.2

[29] R. D. Ball et al., *Parton distributions for the LHC Run II*, JHEP **0**4 (2015) 040, arXiv:1410.8849 [hep-ph]. 5.1.1, 6.2

[30] S. Alioli, P. Nason, C. Oleari, and E. Re, *A general framework for implementing NLO calculations in shower Monte Carlo programs: the POWHEG BOX*, JHEP **0**6 (2010) 043, arXiv:1002.2581 [hep-ph]. 5.1.1, 6.2

[31] A. Ballestrero et al., *Precise predictions for same-sign W-boson scattering at the LHC*, Eur. Phys. J. **C78** (2018) no. 8, 671, arXiv:1803.07943 [hep-ph]. 5.1.1

[32] J. Alwall, R. Frederix, S. Frixione, V. Hirschi, F. Maltoni, O. Mattelaer, H. S. Shao, T. Stelzer, P. Torrielli, and M. Zaro, *The automated computation of tree-level and next-to-leading order differential cross sections, and their matching to parton shower simulations*, JHEP **0**7 (2014) 079, arXiv:1405.0301 [hep-ph]. 5.1.1, 6.2

[33] H.-L. Lai, M. Guzzi, J. Huston, Z. Li, P. M. Nadolsky, J. Pumplin, and C. P. Yuan, *New parton distributions for collider physics*, Phys. Rev. D **82** (2010) 074024, arXiv:1007.2241 [hep-ph]. 5.1.1, 6.2

[34] T. Sjostrand, S. Mrenna, and P. Skands, *PYTHIA 6.4 physics and manual*, JHEP **05** (2006) 026, arXiv:0603175 [hep-ph]. 5.1.1

[35] ATLAS Collaboration, G. Aad et al., *Muon reconstruction performance of the ATLAS detector in protonproton collision data at $\sqrt{s}$ =13 TeV*, Eur. Phys. J. **C76** (2016) no. 5, 292, arXiv:1603.05598 [hep-ex]. 5.2.1.1, 2

[36] ATLAS Collaboration Collaboration, *Electron efficiency measurements with the ATLAS detector using the 2015 LHC proton-proton collision data*, Tech. Rep. ATLAS-CONF-2016-024, CERN, Geneva, Jun, 2016. https://cds.cern.ch/record/2157687. 5.2.1.2

[37] M. Cacciari, G. P. Salam, G. Soyez, *The anti-k_t jet clustering algorithm*, JHEP **0**4 (2008) 063, arXiv:0802.1189 [hep-ph]. 5.2.1.3, 6.4.1

[38] ATLAS Collaboration, M. Aaboud et al., *Jet energy scale measurements and their systematic uncertainties in proton-proton collisions at $\sqrt{s} = 13$ TeV with the ATLAS detector*, Phys. Rev. **D**96 (2017) no. 7, 072002, arXiv:1703.09665 [hep-ex]. 5.2.1.3

[39] *Tagging and suppression of pileup jets with the ATLAS detector*, Tech. Rep. ATLAS-CONF-2014-018, CERN, Geneva, May, 2014. http://cds.cern.ch/record/1700870. 5.2.1.3

[40] D. Adams, C. Anastopoulos, A. Andreazza, M. Aoki, L. Asquith, M. Begel, F. Bernlochner, U. Blumenschein, A. Bocci, S. Cheatham, W. Davey, P.-A. Delsart, P.-O. DeViveiros, A. Dewhurst, D. Duschinger, F. Filthaut, P. Francavilla, F. Garberson, S. Head, A. Henrichs, A. Hoecker, M. Kagan, B. Kersevan, T. Khoo, B. Lenzi, D. Lopez Mateos, B. Malaescu, Z. Marshall, T. Martin, C. Meyer, A. Morley, W. Murray, M. zur Nedden, R. Nicolaidou, S. Pagan Griso, G. Pasztor, P. Petroff, C. Pizio, R. Polifka, X. Poveda, R. Reece, F. Ruehr, F. Salvatore, R. Sandstroem, T. Scanlon, D. Scheirich, S. Schramm, A. Schwartzman, K. Suruliz, M. Sutton, E. Thompson, M. Tripiana, A. Tuna, S. Viel, M. Vincter, I. Vivarelli, M. Wielers, A. Wildauer, and Z. Zinonos, *Recommendations of the Physics Objects and Analysis Harmonisation Study Groups 2014*, Tech. Rep. ATL-PHYS-INT-2014-018, CERN, Geneva, Jul, 2014. https://cds.cern.ch/record/1743654. 5.2.1.4

[41] ATLAS Collaboration, M. Aaboud et al., *Measurement of the cross-section for producing a W boson in association with a single top quark in pp collisions at $\sqrt{s} = 13$ TeV with ATLAS*, JHEP **0**1 (2018) 063, arXiv:1612.07231 [hep-ex]. 5.2.1.4

[42] ATLAS Collaboration, M. Aaboud et al., *Performance of missing transverse momentum reconstruction with the ATLAS detector using proton-proton collisions at $\sqrt{s} = 13$ TeV*, Eur. Phys. J. **C**78 (2018) no. 11, 903, arXiv:1802.08168 [hep-ex]. 5.2.2

[43] ATLAS Collaboration, M. Aaboud et al., *Measurements of b-jet tagging efficiency with the ATLAS detector using $t\bar{t}$ events at $\sqrt{s} = 13$ TeV*, JHEP **0**8 (2018) 089, arXiv:1805.01845 [hep-ex]. 5.2.2

[44] R. Steerenberg, *LHC Report: Another run is over and LS2 has just begun...*, https://home.cern/news/news/accelerators/lhc-report-another-run-over-and-ls2-has-just-begun, 2018. Accessed: 2018-12-14. 6

[45] *Letter of Intent for the Phase-I Upgrade of the ATLAS Experiment*, Tech. Rep. CERN-LHCC-2011-012. LHCC-I-020, CERN, Geneva, Nov, 2011. http://cds.cern.ch/record/1402470. 6

[46] G. Apollinari, I. Bjar Alonso, O. Brning, M. Lamont, and L. Rossi, *High-Luminosity Large Hadron Collider (HL-LHC): Preliminary Design Report*. CERN Yellow Reports: Monographs. CERN, Geneva, 2015. https://cds.cern.ch/record/2116337. 6

[47] ATLAS Collaboration Collaboration, ATLAS Collaboration, *ATLAS Phase-II Upgrade Scoping Document*, Cern-lhcc-2015-020, Geneva, Sep, 2015. http://cds.cern.ch/record/2055248. 6

[48] D. Espriu and B. Yencho, *Longitudinal WW scattering in light of the "Higgs boson" discovery*, Phys. Rev. D **87** (2013) 055017, arXiv:1212.4158 [hep-ph]. 6, 6.1

[49] ATLAS Collaboration Collaboration, *Prospects for the measurement of the $W^{\pm}W^{\pm}$ scattering cross section and extraction of the longitudinal scattering component in pp collisions at the High-Luminosity LHC with the ATLAS experiment*, Tech. Rep. ATL-PHYS-PUB-2018-052, CERN, Geneva, Dec, 2018. http://cds.cern.ch/record/2652447. 6

[50] ATLAS Collaboration Collaboration, *Studies on the impact of an extended Inner Detector tracker and a forward muon tagger on $W^{\pm}W^{\pm}$ scattering in pp collisions at the High-Luminosity LHC with the ATLAS experiment*, Tech. Rep. ATL-PHYS-PUB-2017-023, CERN, Geneva, Dec, 2017. https://cds.cern.ch/record/2298958. 6

[51] T. Sjöstrand, S. Ask, J. R. Christiansen, R. Corke, N. Desai, P. Ilten, S. Mrenna, S. Prestel, C. O. Rasmussen, and P. Z. Skands, *An Introduction to PYTHIA 8.2*, Comput. Phys. Commun. **1**91 (2015) 159–177, arXiv:1410.3012 [hep-ph]. 6.2

[52] ATLAS Collaboration Collaboration, *Expected performance for an upgraded ATLAS detector at High-Luminosity LHC*, Tech. Rep. ATL-PHYS-PUB-2016-026, CERN, Geneva, Oct, 2016. http://cds.cern.ch/record/2223839. 6.3

[53] P. C. Bhat, H. B. Prosper, S. Sekmen, and C. Stewart, *Optimizing Event Selection with the Random Grid Search*, Comput. Phys. Commun. **2**28 (2018) 245–257, arXiv:1706.09907 [hep-ph]. 6.5.1

[54] G. Cowan, K. Cranmer, E. Gross, and O. Vitells, *Asymptotic formulae for likelihood-based tests of new physics*, Eur. Phys. J. **C**71 (2011) 1554, arXiv:1007.1727 [physics.data-an]. [Erratum: Eur. Phys. J.C73,2501(2013)]. 6.5.1